

**Measurement report: Formation and brownness of aqueous secondary organic aerosol from the aged biomass-burning emissions in the Sichuan Basin, China**

1 Chao Peng<sup>1,2,3,4</sup>, Yan Ding<sup>4</sup>, Zhenliang Li<sup>1,2,3</sup>, Tianyu Zhai<sup>4</sup>, Xinping

2 Yang<sup>4</sup>, Mi Tian<sup>6</sup>, Yang Chen<sup>5</sup>, Xin Long<sup>5</sup>, Haohui Tang<sup>6</sup>, Guangming

3 Shi<sup>7</sup>, Liuyi Zhang<sup>8</sup>, Kangyin Zhang<sup>8</sup>, Fumo Yang<sup>7</sup>, and Chongzhi Zhai<sup>1,2,3</sup>

4 <sup>1</sup>Chongqing Academy of Ecology and Environmental Sciences, Chongqing, 401336,  
5 China

6 <sup>2</sup>Chongqing Branch Academy of Chinese Research Academy of Environmental  
7 Sciences, Chongqing, 401336, China

8 <sup>3</sup>Chongqing Key Laboratory of Urban Atmospheric Environment Observation and  
9 Pollution Prevention, Chongqing, 401336, China

10 <sup>4</sup>Chinese Research Academy of Environmental Sciences, Beijing 100012, China

11 <sup>5</sup>Chongqing Institute of Green and Intelligent Technology, Chinese Academy of  
12 Sciences, Chongqing, 400714, China

13 <sup>6</sup>College of Environment and Ecology, Chongqing University, Chongqing, 400045,  
14 China

15 <sup>7</sup>College of Carbon Neutrality Future Technology, Sichuan University, Chengdu,  
16 610065, China

17 <sup>8</sup>Chongqing Three Gorges University, Wanzhou, 404000, China

18 **Correspondence:** Chao Peng (pengchao0623@sina.com) and Chongzhi Zhai  
19 (czz66818@sina.com)

20 **Abstract.** Secondary organic aerosol (SOA) formed via complex chemical  
21 mechanisms was the major contributor to atmospheric aerosol pollution and climate  
22 forcing worldwide. The aqueous-phase oxidation was an important pathway for SOA  
23 formation and the aqueous SOA (aqSOA) exhibited absorption properties across  
24 ultraviolet to visible range. Here, we reported the formation and absorption properties  
25 of aqSOA in the Sichuan Basin, China. aqSOA was originated from the aged  
26 biomass-burning emissions via aqueous-phase reactions instead of photo-chemical  
27 reactions under high aerosol liquid water content (ALWC) conditions, especially  
28 during the polluted period. The substantial impact on brown carbon (BrC) absorption  
29 from SOA was observed from 370 nm to 660 nm (27.5%–43.2%). This study  
30 highlighted the significant contribution of aqSOA formation from aged  
31 biomass-burning emissions to the BrC budget and absorption, especially at night. The  
32 mean aerosol absorption Ångström exponents from 370 nm to 880 nm ( $AAE_{370-880}$ )  
33 was 1.95, higher than that observed in fresh and photo-chemically aged  
34 biomass-burning emissions. This study revealed the aqSOA formation and brownness  
35 from aged biomass-burning emissions and highlighted the importance of  
36 aqueous-phase reactions on aerosol pollution and absorption.

37 **Keywords:** Particulate matter; Secondary organic aerosol; Aqueous-phase oxidation;  
38 Aged biomass-burning emissions; Brown carbon.

## 39 **1 Introduction**

40 Organic aerosol (OA) is the dominant component (20 to 90%) of atmospheric  
41 aerosol with significantly implications for air quality and climate forcing (Jimenez et  
42 al., 2009). Numerous field observations indicated that secondary OA (SOA), formed  
43 by atmospheric oxidation of volatile organic compounds (VOCs) and primary OA  
44 (POA), accounted for most of OA worldwide (Ervens et al., 2011; Huang et al., 2014;  
45 Kourtchev et al., 2016). Recent results showed that aqueous-phase oxidation is an  
46 important pathway for SOA formation and these SOA production (aqSOA) exhibit  
47 absorption properties across ultraviolet (UV) to visible (Vis) range (Gilardoni et al.,  
48 2016; Lim et al., 2010; McNeill 2015; Powelson et al., 2014; Sun et al., 2010).  
49 However, the formation mechanisms and absorption properties of aqSOA are poorly  
50 understood, hindering to improvement of air quality and reducing the uncertainties in  
51 global climate estimations.

52 An increasing number of studies pointed toward aqSOA as a major SOA could  
53 form in fogs, clouds, and aerosol water (Ervens et al., 2011; Ortiz-Montalvo et al.,  
54 2012; Tan et al., 2012; Xu et al., 2022). And the oxygenated VOCs (OVOCs) with  
55 large water-soluble and low Henry's constant (i.e., methylglyoxal and glycolaldehyde)  
56 are the important aqSOA precursors (Ortiz-Montalvo et al., 2012; Tan et al., 2012). A  
57 few laboratory studies investigated the levoglucosan and phenolic species produced  
58 from biomass burning could also act as aqSOA precursors (Yu et al., 2016; Zhao et al.,  
59 2014). Gilardoni et al. (2016) reported direct ambient observations of aqSOA  
60 formation from biomass-burning emissions in fog water and wet aerosol. Additionally,  
61 recent studies indicated that aqSOA with high molecular weight (i.e., 4-ethylphenol)  
62 formed by aqueous-phase photochemical oxidation showed strong light absorptivity  
63 within UV range (Herrmann et al., 2015; Ye et al., 2019). Previous laboratory studies  
64 also demonstrated that aqSOA, such as  $\pi$ -conjugated compounds and imidazole with  
65 C=N bonds produced by aldol condensation and aqueous-phase carbonyl compound  
66 reactions respectively, would strongly absorb light at near-UV (Drozd and McNeill,  
67 2014; Kampf et al., 2012; Nozière and Esteve, 2007; Powelson et al., 2014). Despite

68 numerous studies reported on the formation and optical properties of aqSOA, limited  
69 research on its ambient observations hinder to better understand the role of aqSOA in  
70 atmospheric chemistry and climate.

71 China experienced severe PM<sub>2.5</sub> pollution under the stagnant high-humidity  
72 conditions, when SOA as the major component was originated from fossil fuel  
73 combustion and biomass burning (Huang et al., 2014; Wang et al., 2016; Wang et al.,  
74 2021; Xu et al., 2022). Field observations indicated that highly oxidized SOA could  
75 form through aqueous-phase processing driven by acid-catalyzed oxidation (Meng et  
76 al., 2020; Xu et al., 2017), and aqSOA is formed from biomass-burning OA (BBOA)  
77 and fossil-fuel OA via aqueous-phase reactions (Wang et al., 2021; Zhao et al., 2019).  
78 A few laboratory studies found aqueous-phase reactions were an important oxidation  
79 pathway for nitrophenol products (i.e., 5-nitrovanillin and 4-nitroguaiacol) with strong  
80 UV absorption and higher formation and transformation rates were observed in more  
81 acidic solutions (Kroflc et al., 2015; Li et al., 2023; Pang et al., 2019; Yang et al.,  
82 2021). However, observations on aqSOA formation and optical properties in China  
83 are limited and most research concentrate on the North China Plain (NCP). Similar to  
84 NCP, the Sichuan Basin (SCB) characterized by high humidity and frequent biomass  
85 burning is also the main region with severe aerosol pollution in China (Tian et al.,  
86 2019; Wang et al., 2018; Yang et al., 2011). Previous research indicated that aqSOA  
87 from different regions exhibited distinct formation mechanisms and optical properties,  
88 due to the diverse sources and ambient conditions (Bao et al., 2023; Bao et al., 2024;  
89 Wang et al., 2021; Xu et al., 2017). For instance, Wang et al. (2021) revealed fast  
90 aqueous-phase conversion of fossil-fuel primary organic aerosol (FF-POA) to aqSOA  
91 under high-humidity conditions during a Beijing winter haze event, and found that  
92 aqSOA exhibited much lower light absorption than its primary precursor due to  
93 decreased aromaticity. Similarly, Huang et al. (2023) illustrated that the  
94 aqueous-phase oxidation of fossil fuel combustion emissions played a critical role in  
95 SOA formation under high RH conditions. Unlike these studies in NCP, the effect of  
96 aqueous-phase reactions on oxygenated OA (OOA) formation was significant when  
97 aerosol liquid water content (ALWC) was below 200  $\mu\text{g m}^{-3}$ , but was insignificant

98 when ALWC > 200  $\mu\text{g m}^{-3}$  in SCB. Additionally, the aqueous-phase oxidation process  
99 probably did not play a role in the decay of BrC during summer in Chengdu (Bao et  
100 al., 2024). Currently, few studies explored the dynamic evolution and optical  
101 properties of aqSOA, and the knowledge of ambient aqSOA processing is still limited  
102 in SCB. Therefore, a more detailed characterization of aqSOA formation and optical  
103 properties is of great importance to reveal the key factors contributing to haze  
104 formation.

105 Here a time-of-flight aerosol chemical speciation monitor (ToF-ACSM) and a  
106 series of collocated instruments were used to characterize aqSOA dynamic evolution  
107 from biomass burning under real ambient conditions in a typical city with relatively  
108 serious air pollution in SCB from October 21 to November 23, 2022. We observed  
109 that the haze formation was largely driven by BBOA and aqSOA. We demonstrated  
110 aqSOA was originated from the aged BBOA via aqueous-phase reactions. Finally, we  
111 further showed that aqSOA produced from aged BBOA were strong UV absorption  
112 with positive radiative forcing. These results revealed the aqSOA formation and  
113 brownness from aged biomass-burning emissions and helped simulate the associated  
114 influences on atmospheric chemistry and climate.

## 115 **2 Methods**

### 116 **2.1 Sampling site**

117 An intensive field campaign on the chemical and physical properties of aerosol  
118 was conducted at a measurement site in a city affected by severe aerosol pollution  
119 (Yongchuan, 29°21'25" N, 105°54'6" E) from October 21 to November 23, 2022. This  
120 is a typical urban site surrounded by restaurants, shopping malls, and residential  
121 buildings, and the site is located in a parallel ridge-and-valley area between two  
122 megacities in SCB (Chongqing center and Chengdu) (Fig. S1). It was primarily  
123 influenced by multiple local emissions from traffic (arterial roads to the east 600 m  
124 and west 300 m) and a variety of residential sources (i.e., biomass burning and fossil  
125 fuel combustion). There was no interference of dynamics from neighboring buildings,

126 and measurements at the site helped understand the characteristics of haze pollution  
127 dynamic evolution.

## 128 **2.2 Instrumentation**

129 During the campaign, the non-refractory aerosol (NR-PM<sub>2.5</sub>) species, including  
130 OA, ammonium (NH<sub>4</sub>), nitrates (NO<sub>3</sub>), sulfates (SO<sub>4</sub>), and chlorides (Chl), were  
131 measured on-line by ToF-ACSM (Aerodyne Research Inc.). Ambient aerosols were  
132 pumped into ToF-ACSM at a flow rate of 3 L min<sup>-1</sup> through a PM<sub>2.5</sub> cyclone  
133 (URG-2000-30ED) and a Nafion dryer (MD-110-48S, Perma Pure, Inc.) reducing the  
134 relative humidity to below 30%. The measurement principle was described in detail in  
135 the previous studies (Fröhlich et al., 2013; Ng et al., 2011c).

136 A seven-wavelength Aethalometer (AE33, Magee Scientific) was used to  
137 measure the aerosol light absorption (Abs<sub>λ</sub>) and equivalent black carbon (BC<sub>λ</sub>) mass  
138 concentrations in real time at 370, 470, 520, 590, 660, 880, and 950 nm. The sampled  
139 particles were dried by a Nafion dryer (MD-70024S-3, Perma Pure, Inc.) before  
140 entering into AE33. The light attenuation coefficients were converted to Abs<sub>λ</sub> based  
141 on the real-time compensation parameter, and the nonlinear loading effects of quartz  
142 filters were dealt with on-line by the parallel measurements of attenuation values  
143 (ATN1 and ATN2) (Coen et al., 2010; Drinovec et al., 2015). The scattering effects of  
144 quartz filters were modified automatically by a fixed multiple scattering parameter  
145 (2.14). Detailed measurement methods and principles of AE33 can be found in  
146 Drinovec et al. (2015).

147 During the campaign, the gaseous species (including O<sub>3</sub>, NO<sub>2</sub>, and CO) were  
148 continuously measured by gas analyzers (49i, 42i, and 48i, Thermo Scientific), that  
149 were maintained and calibrated weekly. Hourly meteorological parameters data  
150 including temperature (T), relative humidity (RH) and PM<sub>2.5</sub> mass concentrations  
151 were obtained on-line from the measurements at the National Environmental  
152 Monitoring Station, which was close to our sampling site (<http://www.cnemc.cn/>).

## 153 **2.3 Data analysis**

### 154 **2.3.1 ToF-ACSM data analysis**

155 The raw mass spectra data measured by ToF-ACSM were analyzed using  
156 Tofware v2.5.13 (Tofwerk AG) in Igor Pro 6.37 (WaveMetrics, Inc.). The ionization  
157 efficiency (IE) and relative ionization efficiency (RIEs) were regularly calibrated  
158 using a scanning mobility particle sizer with a differential mobility analyzer (SMPS  
159 3081A, TSI) and a condensation particle counter (CPC 3775, TSI). The  
160 comprehensive overview of the operation and calibration procedures of ToF-ACSM  
161 can be found in Bao et al. (2023). In accordance with previous studies, the default  
162 RIEs values for OA, NO<sub>3</sub>, and Chl were set to 1.4, 1.1, and 1.3, respectively  
163 (Canagaratna et al., 2007; Elser et al., 2016). The IE value (236 ions pg<sup>-1</sup>) and RIEs of  
164 SO<sub>4</sub> (1.2) and NH<sub>4</sub> (4.3) were estimated from the calibrations of pure ammonium  
165 nitrate and ammonium sulfate, respectively. Meanwhile, a particle collection  
166 efficiency (CE) was introduced to compensate for the particle loss, as the acidity, the  
167 contribution of ammonium nitrate (ANMF) and phase state changed the particle  
168 bounce effects at the vaporiser (Matthew et al., 2008). Middlebrook et al. (2012)  
169 developed a CE algorithm for ToF-ACSM to quantify the aerosol species. Their  
170 results indicated that a constant CE value of 0.45 should be used when: (1) the ANMF  
171 is below 40%, or (2) particles are partially or fully neutralized. In this study, aerosol  
172 particles were dried by Nafion dryer (RH < 30%) before sampling by ToF-ACSM,  
173 and the ANMF was always below 40%. As shown in Fig. S2, the average ratio of the  
174 measured NH<sub>4</sub> to the predicted NH<sub>4</sub> needed to fully neutralize the SO<sub>4</sub>, NO<sub>3</sub> and Chl  
175 was approximately 1. All of these conditions did not affect the CE value that had  
176 usually been used at this site. The typical default CE value (0.5) was applied during  
177 the whole sampling period, which was consistent with previous research (Bao et al.,  
178 2025; Peng et al., 2025; Sun et al., 2016a; Sun et al., 2016b; Zhao et al., 2019). While  
179 the typical default CE is 10% higher than 0.45, the difference is small considering the  
180 30% uncertainty determined for CE (Bahreini et al., 2009). Additionally, the strong

181 correlation between NR-PM<sub>2.5</sub> and PM<sub>2.5</sub> mass concentrations supported that the CE  
182 value was reasonable (Fig. S3).

183 The mass spectral matrix of OA for m/z 10–120 was analyzed by positive matrix  
184 factorization (PMF) and multilinear engine (ME2) implemented with the SoFi (Source  
185 Finder) (version 6.3, Canonaco et al., 2013; Paatero 1999; Paatero and Tapper 1994).  
186 Briefly, unconstrained PMF was used to determine the numbers and types of source  
187 factors, then the restriction method ME2 was used to minimize PMF rotational  
188 ambiguity by the *a*-values from 0 to 1 with a step of 0.1 (Elser et al., 2016; Wang et  
189 al., 2019b; Zhong et al., 2021). The ions data with signal-to-noise (S/N) lower than  
190 0.2 were discarded, and those S/N from 0.2–2 were downweighted by a factor of 2  
191 (Bao et al., 2023; Paatero and Hopke 2003). Finally, five OA factors with function of  
192 the rotational parameter ( $f_{\text{peak}} = 0$ ) were identified, including three POA factors (i.e.,  
193 BBOA, coal-combustion OA (CCOA), and hydrocarbon-like OA (HOA)) and two  
194 SOA factors (i.e., OOA and aqSOA) (Fig. S9 and S10). We present detailed diagnostic  
195 plots of the PMF results in the supporting information (Fig. S4–S10). The details of  
196 OA source apportionment procedures are described in SI Text S1.

### 197 **2.3.2 Aerosol liquid water content**

198 The ALWC is controlled by meteorological conditions (T and RH) and also by  
199 inorganic and organic components. During the campaign, the ALWC with inorganic  
200 species was estimated by the ISORROPIA-II model based on the ammonium, nitrates,  
201 sulfates, and chlorides mass concentrations from ToF-ACSM and the meteorological  
202 parameters (T and RH) from National Environmental Monitoring Station (Fountoukis  
203 and Nenes, 2007). Here, the forward type and metastable mode were used in the  
204 ISORROPIA-II model (Hennigan et al., 2015). The thermodynamic equilibrium of the  
205 NH<sub>4</sub><sup>+</sup>–SO<sub>4</sub><sup>2-</sup>–NO<sub>3</sub><sup>-</sup>–Cl<sup>-</sup>–H<sub>2</sub>O system was modeled and ALWC was then calculated.  
206 Consistent with previous research, the organic contribution for ALWC was calculated  
207 by Zdanovskii–Stokes–Robinson (ZSR) mixing rule as discussed in SI Text S2 (Guo  
208 et al., 2015; Huang et al., 2020; Nguyen et al., 2016; Xu et al., 2022). In this study, the

209 ALWC with organic species ranged from 0.1 to 35.2  $\mu\text{g m}^{-3}$ , with an average of  $1.9 \pm$   
210  $3.0 \mu\text{g m}^{-3}$ , taking up  $3.7 \pm 2.2\%$  of total ALWC. As organic species had minor effects  
211 on total ALWC ( $< 5\%$ ), the ALWC was determined only considering inorganic species  
212 (Chen et al., 2021; Guo et al., 2015; Liu et al., 2017).

### 213 2.3.3 Light absorption measurements

214 The  $\text{Abs}_\lambda$  was divided into BC and brown carbon (BrC, a group of colored OA  
215 compounds) absorption ( $\text{Abs}_{\lambda,\text{BC}}$  and  $\text{Abs}_{\lambda,\text{BrC}}$ ) ( $\text{Abs}_\lambda = \text{Abs}_{\lambda,\text{BC}} + \text{Abs}_{\lambda,\text{BrC}}$ ) and  
216 characterized by the absorption Ångström exponents (AAE) (Laskin et al., 2015).  
217 Here,  $\text{Abs}_\lambda$  was determined dependent  $\text{BC}_\lambda$  mass concentrations ( $\text{Abs}_\lambda = \text{BC}_\lambda \times \text{MAC}_\lambda$ ).  
218 We assumed the mass absorption cross-section of aerosols ( $\text{MAC}_\lambda$ ) were 18.47, 14.54,  
219 13.14, 11.58, 10.35, 7.77, and 7.19  $\text{m}^2 \text{g}^{-1}$  at 370, 470, 520, 590, 660, 880, and 950  
220 nm, respectively (Drinovec et al., 2015; Zhu et al., 2017). Here, we assumed that  
221  $\text{Abs}_{880}$  was sole from BC, then the following formula was used to determine  $\text{Abs}_{\lambda,\text{BC}}$   
222 values:  $\text{Abs}_{\lambda,\text{BC}} = \text{Abs}_{880} \times (880/\lambda)^{-\text{AAE}_{\text{BC}}}$  (Drinovec et al., 2015; Kirchstetter and  
223 Novakov, 2004; Moosmüller et al., 2009; Qin et al., 2018; Zhu et al., 2017). The AAE  
224 of BC ( $\text{AAE}_{\text{BC}}$ ) value was obtained from the equality:  
225  $\text{AAE}_{\text{BC}} = -\log_{10}(\text{Abs}_{880}/\text{Abs}_{950}) \div \log_{10}(880/950)$  (Wang et al., 2021). A detailed  
226 description of  $\text{Abs}_{\lambda,\text{BC}}$  and  $\text{Abs}_{\lambda,\text{BrC}}$  calculations is provided in SI Text S3. Previous  
227 research have demonstrated that  $\text{AAE}_{\text{BC}}$  is sensitive to the refractive index, size  
228 distribution, and coating of carbonaceous aerosols (Gyawali et al., 2009; Lack and  
229 Langridge, 2013; Li et al., 2019). In this study, the uncertainty associated with the  
230 estimation of  $\text{Abs}_{\text{BC}}$  and  $\text{Abs}_{\text{BrC}}$  was analyzed (Text S3). The relative uncertainty  
231 ranges of  $\text{Abs}_{\text{BC}}$  and  $\text{Abs}_{\text{BrC}}$  were  $[-46\%, +21\%]$  and  $[-112\%, +42\%]$  at 370 nm,  
232 respectively.  $\text{Abs}_{\lambda,\text{BrC}}$  was caused by primary and secondary BrC light absorption  
233 ( $\text{Abs}_{\lambda,\text{BrC,pri}}$  and  $\text{Abs}_{\lambda,\text{BrC,sec}}$ ). The  $\text{Abs}_{\lambda,\text{BrC,sec}}$  value was calculated by a minimum  
234 R-squared (MRS) method at each wavelength (Wang et al., 2019b; Wu and Yu, 2016;  
235 Wu et al., 2024). The detailed information of MRS method and  $\text{Abs}_{\lambda,\text{BrC,sec}}$  estimation  
236 is provided in SI Text S3.

237 The multiple linear regression (MLR) method was used to analyze the light  
238 absorption of different OA components at each wavelength:  
239  $Abs_{BrC} = a \times [OOA] + b \times [BBOA] + c \times [CCOA] + d \times [aqSOA] + e \times [HOA]$  (Qin et al., 2018;  
240 Xie et al., 2019). The [OOA], [BBOA], [CCOA], [aqSOA], and [HOA] indicated the  
241 mass concentrations of OA species; the a–e were constants, used to optimize the  $Abs_{\lambda}$   
242 of each OA component, and equivalent to MAC values at each wavelength (i.e., a–e at  
243 370 nm represented  $MAC_{370,OOA}$ ,  $MAC_{370,BBOA}$ ,  $MAC_{370,CCOA}$ ,  $MAC_{370,aqSOA}$ , and  
244  $MAC_{370,HOA}$ , respectively). Here, the normalized mean bias (NMB), root mean square  
245 error (RMSE), and index of agreement (IOA) were used to evaluate the performance  
246 of the MLR method (SI Text S4) (Li et al., 2011). The IOA values of  $Abs_{370,BrC}$  and  
247  $Abs_{470,BrC}$  (0.99 and 1.00) exceeded 0.95. The slopes of the relationship between  
248  $Abs_{370,BrC}$  and  $Abs_{470,BrC}$  measured by AE33 and estimated by MLR method were 0.81  
249 and 0.96 (close to unity), respectively. These results indicated a good agreement of  
250  $Abs_{370,BrC}$  between AE33 measurement and the MLR reconstruction.

## 251 **3 Results and discussion**

### 252 **3.1 General descriptions**

253 The temporal variations of  $PM_{2.5}$  species concentrations, meteorological  
254 parameters,  $Abs_{370,BrC}$  and  $MAC_{370,BrC}$  during the campaign are shown in Fig. 1. The  
255 winds were weak with  $0.3 \pm 0.2 \text{ m s}^{-1}$  over the whole campaign, indicating the  
256 atmosphere was in stagnant conditions. The total  $PM_{2.5}$  (BC+NR- $PM_{2.5}$ ) mass  
257 concentrations ranged from 7.0 to 175.5  $\mu\text{g m}^{-3}$ , with an average of  $48.4 \pm 27.8 \mu\text{g}$   
258  $\text{m}^{-3}$  during the campaign. The average concentrations of OA,  $\text{NO}_3$ ,  $\text{SO}_4$ ,  $\text{NH}_4$ , Chl,  
259 and BC were  $24.1 \pm 18.1$ ,  $8.3 \pm 6.2$ ,  $6.2 \pm 3.4$ ,  $5.2 \pm 2.7$ ,  $0.2 \pm 0.1$ , and  $4.7 \pm 2.9 \mu\text{g}$   
260  $\text{m}^{-3}$ , taking up  $46.6 \pm 10.7\%$ ,  $17.7 \pm 8.0\%$ ,  $13.2 \pm 4.4\%$ ,  $11.2 \pm 2.7\%$ ,  $0.3 \pm 0.2\%$ , and  
261  $10.1 \pm 5.5\%$  of total  $PM_{2.5}$ , respectively. OA constituted the largest fraction of total  
262  $PM_{2.5}$ , highlighting the importance of OA in  $PM_{2.5}$  pollution in SCB (Bao et al., 2023;  
263 Wang et al., 2018). Meanwhile, the high values of  $Abs_{370,BrC}$  and  $MAC_{370,BrC}$ , ranging  
264 from 5.8 to 210.2  $\text{Mm}^{-1}$  ( $42.4 \pm 28.5 \text{ Mm}^{-1}$ ) and from 0.6 to 7.0  $\text{m}^2 \text{g}^{-1}$  ( $2.1 \pm 0.9 \text{ m}^2$

265 g<sup>-1</sup>) respectively, were observed during the campaign.

266 According to the Chinese National Ambient Air Quality Standard (NAAQS) (GB  
267 3095-2012) (MEP, 2012), the Grade I and Grade II levels for daily PM<sub>2.5</sub> mass  
268 concentration are 35 μg m<sup>-3</sup> and 75 μg m<sup>-3</sup>, respectively. The Chinese NAAQS Grade  
269 II level, based on WHO's Phase-1 interim target (IT-1), is higher than the WHO Air  
270 Quality Guideline (AQG) value (15 μg m<sup>-3</sup>), the EU daily limit (25 μg m<sup>-3</sup>), and U.S.  
271 24-hour standard (35 μg m<sup>-3</sup>). During the campaign, the average of PM<sub>2.5</sub> mass  
272 concentration was 1.4 times NAAQS Grade I level (35 μg m<sup>-3</sup>). Therefore, the  
273 pollution periods (PP) were defined by the daily PM<sub>2.5</sub> mass concentration exceeding  
274 NAAQS Grade II level of 75 μg m<sup>-3</sup>. Similarly, the days with PM<sub>2.5</sub> mass  
275 concentration below 75 μg m<sup>-3</sup> were characterized as clean periods (CP). During PP,  
276 the mass concentrations of BC+NR-PM<sub>2.5</sub> and OA were 102.3 ± 26.9 and 57.4 ± 22.5  
277 μg m<sup>-3</sup>, 2.5 and 3.1 times that during CP, respectively. As shown in Fig. 2, the PM<sub>2.5</sub>  
278 species were substantially different in the PP and CP. Compared with other species, a  
279 significantly higher contribution of OA was observed during PP (56.6%) than CP  
280 (46.6%) (Student's t-test, *p* < 0.001) (Fig. 2). Here, five OA factors were identified by  
281 the PMF model with detailed information in SI Text S1, and the mass spectrum of  
282 these factors is shown in Fig. S9. HOA mass spectrum was characterized by alkyl  
283 fragment ion series at C<sub>n</sub>H<sup>+</sup><sub>2n-1</sub> and C<sub>n</sub>H<sup>+</sup><sub>2n+1</sub> (i.e., *m/z* 41, 43, 55, and 57), they are  
284 common characteristics of primary combustion emissions (Elser et al., 2016; Lanz et  
285 al., 2007). BBOA was identified by the high signal of *m/z* 60 (mainly C<sub>2</sub>H<sub>4</sub>O<sub>2</sub><sup>+</sup>) and  
286 *m/z* 73 (mainly C<sub>3</sub>H<sub>5</sub>O<sub>2</sub><sup>+</sup>), they are the fragments of levoglucosan and mannosan  
287 emitted from incomplete biomass burning (Alfarra et al., 2007). CCOA had high  
288 correlation with the unsaturated hydrocarbon ion fragments such as PAH-related ion  
289 fragments (i.e., *m/z* 77, 91, 115), emitted from traditional coal combustion (Sun et al.,  
290 2016a). OOA was distinguished by the prominent signal of *m/z* 44 (mainly CO<sub>2</sub><sup>+</sup>) and  
291 highly correlated with the oxygenated ions (Ng et al., 2011b). aqSOA also had high  
292 correlation with the oxygenated ions (i.e., *m/z* 43 (mainly C<sub>2</sub>H<sub>3</sub>O<sup>+</sup>) and *m/z* 44).  
293 The mass spectrum of aqSOA showed a significantly higher *m/z* 29 (mainly CHO<sup>+</sup>)  
294 signal than other OA factors, consistent with those reported in the previous studies

295 (Sun et al., 2016a; Xu et al., 2019; Zhao et al., 2019; Zhong et al., 2021). Moreover,  
296 BBOA showed significant correlations with m/z 60 (mainly  $C_2H_4O_2^+$ ) and m/z 73  
297 (Pearson's  $r^2$  ( $r^2$ ) = 0.85, 0.80,  $p < 0.001$ ); CCOA was strongly correlated with Chl  
298 and m/z 115 ( $r^2 = 0.56, 0.48, p < 0.001$ ); HOA was correlated with  $NO_2$  and m/z 41  
299 ( $r^2 = 0.47, 0.59, p < 0.001$ ); OOA and aqSOA were significantly correlated with  $NO_3$ ,  
300  $NH_4$  ( $r^2 = 0.77, 0.75, p < 0.001$ ) and  $SO_4$ , ALWC ( $r^2 = 0.67, 0.85, p < 0.001$ ),  
301 respectively (Fig. S10). These results highlighted the result of five OA factors was  
302 reasonable.

303 It should be noted that the contributions of BBOA and aqSOA to OA increased  
304 from CP (31.7% and 12.6%) to PP (38.6% and 14.1%), while CCOA, HOA, and OOA  
305 contributions decreased. Additionally, significantly higher RH and ALWC were  
306 observed during PP ( $58.5 \pm 12.4\%$  and  $69.4 \pm 30.3 \mu g m^{-3}$ ) than CP ( $49.8 \pm 8.9\%$  and  
307  $37.1 \pm 20.8 \mu g m^{-3}$ ) ( $p < 0.001$ ), but not temperature ( $p > 0.1$ ). The wind was  $0.32 \pm$   
308  $0.18 m s^{-1}$  during CP, 1.3 times that during PP. These results indicated that the  
309 atmosphere was in a stagnant state with relatively high RH and ALWC during PP,  
310 which might lead to the largely different sources and chemical processing of OA  
311 during CP and PP. Compared with CP, the obvious diurnal variation of OA  
312 concentration was exhibited during PP. As shown in Fig. 2, the OA concentration peak  
313 ( $82.7 \mu g m^{-3}$ ) was observed at 12:00 local time (LT) in the daytime during PP, while  
314 observed at 21:00 LT at night during CP. Moreover, OA concentration rapidly  
315 increased at a rate of  $7.8 \mu g m^{-3} hr^{-1}$  from 09:00 to 12:00 LT with a significant  
316 decrease of  $NO_3$  during PP. Meanwhile, BBOA and aqSOA concentrations showed  
317 similar diurnal patterns to OA concentration with high values in the daytime and  
318 rapidly increased from 09:00 to 12:00 LT during PP. Previous research indicated that  
319 aqSOA spectrum showed higher m/z 29 ( $CHO^+$ ) than other OA factors (Gilardoni et  
320 al., 2016; Meng et al., 2020; Wang et al., 2021). During PP, the peaks of m/z 60 and  
321 m/z 29 concentrations, tracer ion fragments of BBOA and aqSOA, were observed at  
322 12:00 LT ( $1.2 \mu g m^{-3}$ ) and 13:00 LT ( $4.3 \mu g m^{-3}$ ), respectively. Additionally, the  
323 correlation between ALWC and aqSOA concentrations ( $r^2 = 0.86, p < 0.001$ ) was  
324 stronger than BBOA concentrations ( $r^2 = 0.58, p < 0.001$ ), and both ALWC and

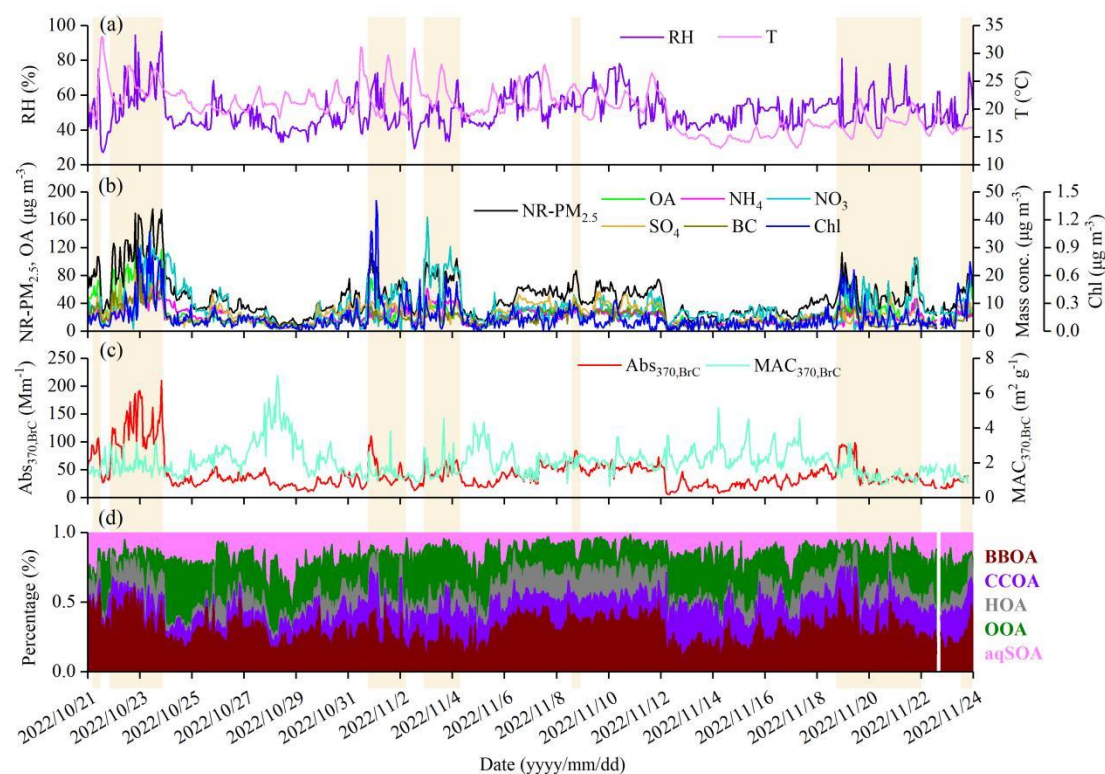
325 aqSOA concentration peaks were observed at 13:00 LT, earlier than BBOA  
326 concentration peak (12:00 LT), supporting that ALWC might play a significant role in  
327 the chemical processing of aqSOA formation from BBOA during PP. In contrast, the  
328 odd oxygen ( $O_x = O_3 + NO_2$ ) showed weak correlations with both OOA and aqSOA  
329 concentrations during the campaign ( $p > 0.1$ ) (not shown). Although the average  $O_x$   
330 concentration was higher during PP ( $51.1 \pm 19.6$  ppb) than CP ( $36.9 \pm 14.0$  ppb), no  
331 significant correlations were observed in either period (not shown). These results  
332 suggested that photochemical reactions might played a limited role in SOA formation  
333 in this study.

334 In summary, these results suggested that OA was the dominant component of  
335  $PM_{2.5}$ , especially during PP in SCB. During PP, BBOA and aqSOA played important  
336 roles in increasing OA concentration in the daytime. Previous research indicated that  
337 the autumn harvest period – specifically October and November – is a period of  
338 intensified biomass burning in SCB, primarily due to post-harvest crop residue  
339 burning (Chen et al., 2017; Tao et al., 2014). Thus, aqSOA in the daytime during PP  
340 might be related to the high aerosol water and BBOA emissions (Bao et al., 2023;  
341 Chen et al., 2017; Chen et al., 2019; Tao et al., 2014). Additionally, Gilardoni et al.  
342 (2016) also found that aqSOA such as guaiacol dimer ( $C_{14}H_{14}O_4^+$ ) could be formed  
343 from aged biomass-burning emissions at both in fog water and in wet aerosol,  
344 especially under high ALWC conditions. To further explore aqSOA formed from  
345 biomass-burning emissions via the aqueous-phase reactions, the next section would  
346 discuss the dynamic evolution of aqSOA in relation to BBOA.

删除[臻予祝愿]: Additionally, considerable

删除[臻予祝愿]: in the harvest season – autumn – in SCB

删除[臻予祝愿]: Based on the direct observation of aqSOA,

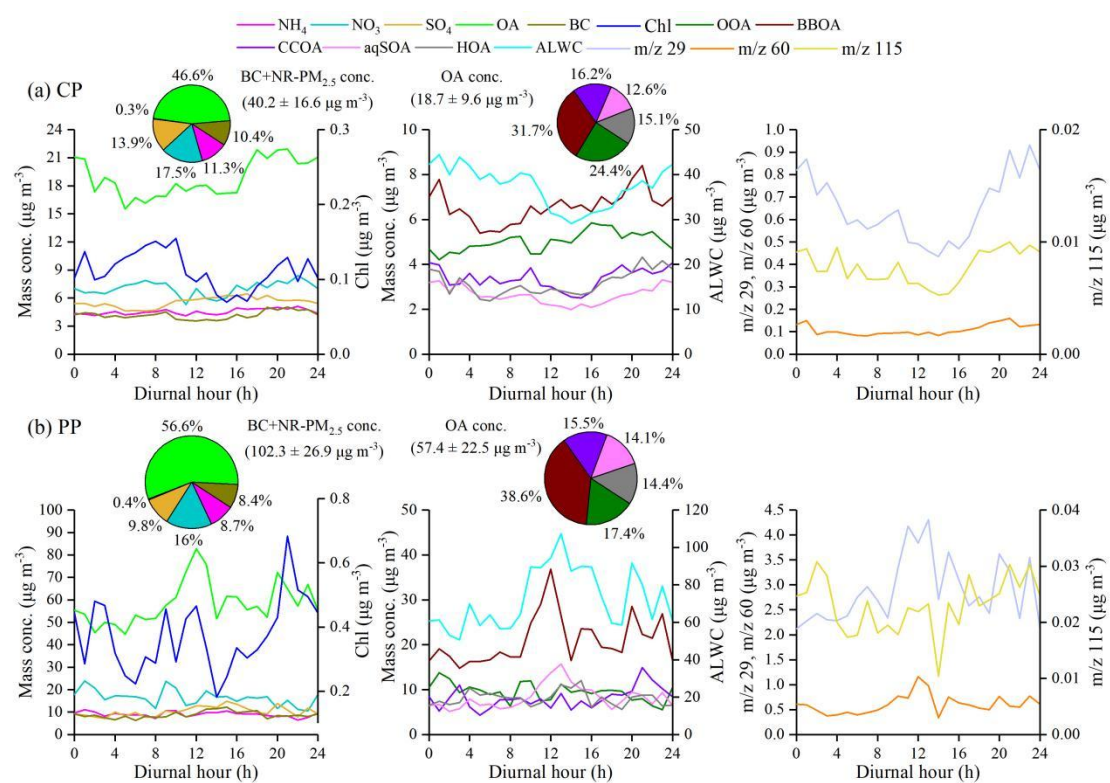


347

348 **Figure 1.** Time series of (a) RH and T, (b) NR-PM<sub>2.5</sub> species measured by ToF-ACSM and BC, (c)

349 Abs<sub>370,BrC</sub> and MAC<sub>370,BrC</sub>, and (d) mass fraction of OA factors during the campaign. The pollution

350 period (BC+NR-PM<sub>2.5</sub> > 75 µg m<sup>-3</sup>) is highlighted by the shaded areas.



351

352 **Figure 2.** Diurnal variations of PM<sub>2.5</sub> species, BC, OA factors, m/z 29, m/z 60, and m/z 115 mass

353 concentrations during **(a)** clean period (CP) ( $BC+NR-PM_{2.5} < 75 \mu g m^{-3}$ ) and **(b)** polluted period  
354 (PP) ( $BC+NR-PM_{2.5} > 75 \mu g m^{-3}$ ). The pie charts in the left side of **(a)** and **(b)** show the average  
355 mass contributions of different chemical compositions to  $BC+NR-PM_{2.5}$  during CP and PP,  
356 respectively. Meanwhile, the average mass contributions of OOA, BBOA, CCOA, aqSOA, and  
357 HOA in OA are shown in the pie charts in the middle of **(a)** and **(b)**, respectively.

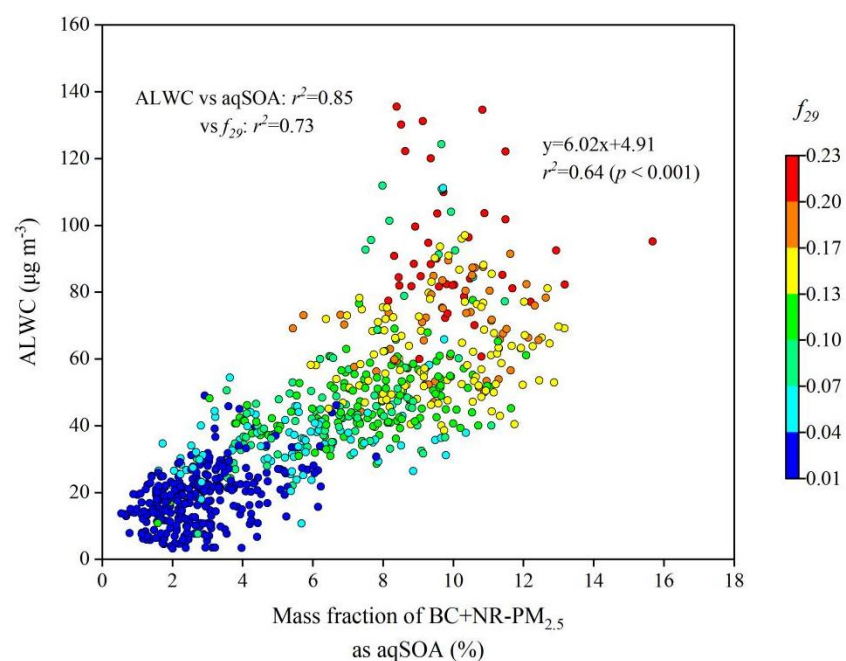
### 358 **3.2 Biomass-burning emissions as precursors for aqSOA**

359 Fig. 3 shows the strong correlation between the mass fraction (%) of aqSOA in  
360 total  $PM_{2.5}$  and ALWC during the campaign ( $r^2 = 0.64, p < 0.001$ ). The contribution of  
361 aqSOA increased with the increase of  $f_{29}$  values (normalized mass spectrum signal at  
362  $m/z$  29). It was important to note that the aqSOA factor showed significantly higher  
363  $f_{29}$  and  $f_{60}$  values (normalized mass spectrum signal at  $m/z$  60) (0.167 and 0.011) than  
364 the OOA factor (0.017 and 0.002), respectively (Fig. S9). Moreover, both aqSOA  
365 concentrations and  $f_{29}$  were well correlated with ALWC ( $r^2 = 0.85, 0.73, p < 0.001$ )  
366 (Fig. 3). During the campaign, the average value of the oxygen-to-carbon ratio (O:C)  
367 of aqSOA factor (0.85) was 2.7 times that (0.31) of BBOA factor. However, the  
368 similar hydrogen-to-carbon ratio (H:C) values of aqSOA factor and BBOA factor  
369 were observed (1.74 and 1.81, respectively), indicating that a hydrogen atom might be  
370 replaced by a OH moiety (Lim et al., 2010; Ng et al., 2011a). These results were  
371 similar to aqSOA observed in Italy and Beijing (Gilardoni et al., 2016; Zhao et al.,  
372 2019). Additionally, previous studies indicated that aqueous-phase processes could  
373 play a role in the formation of SOA from fossil fuel emissions (Ervens et al., 2011;  
374 Huang et al., 2023; Wang et al., 2021; Xu et al., 2022; Yan et al., 2017). For example,  
375 Wang et al. (2021) and Xu et al. (2022) have highlighted the potential for  
376 aqueous-phase reactions to contribute to SOA formation, particularly in regions with  
377 high levels of anthropogenic emissions. In this study, a strong anticorrelation between  
378 the mass fraction of fossil-fuel related OA components (sum of CCOA, HOA and  
379 OOA) and ALWC at the high  $f_{29}$  values was also observed ( $r^2 = 0.48, p < 0.001$ ) (not  
380 shown), consistent with recent research (Wang et al., 2021). This indicated that

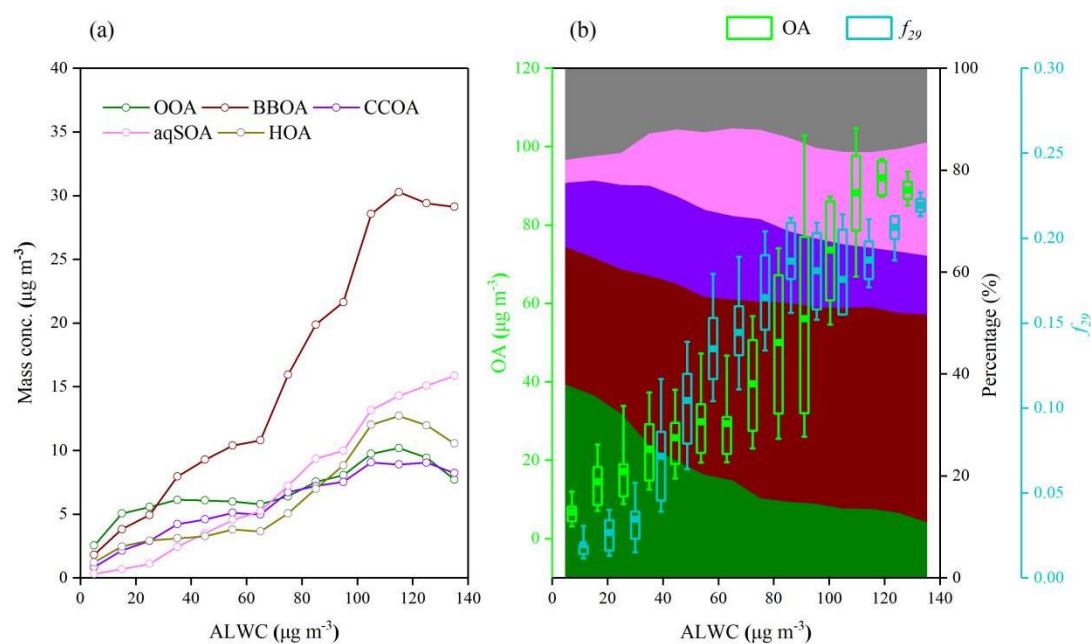
381 aqSOA might also be produced by aqueous-phase reactions of fossil-fuel related OA  
382 components.

383 Fig. 4 shows the relationships between ALWC and OA factors or  $f_{29}$  during the  
384 campaign. Five OA factors mass concentrations increased with the increase of ALWC.  
385 However, compared with other OA factors, aqSOA and BBOA significantly increased  
386 from 1.1 and 4.9  $\mu\text{g m}^{-3}$  to 5.2 and 10.8  $\mu\text{g m}^{-3}$  when  $20 \mu\text{g m}^{-3} < \text{ALWC} < 60 \mu\text{g m}^{-3}$ ,  
387 respectively. It should be noted that only aqSOA concentrations were  
388 enhancement under high ALWC conditions ( $> 100 \mu\text{g m}^{-3}$ ). It is likely because more  
389 water-soluble organic species (i.e., glyoxal and methylglyoxal) were formed, that  
390 were further oxidized to form aqSOA via aqueous-phase reactions in aerosol liquid  
391 water (Carlton et al., 2007; Ervens et al., 2011; Tan et al., 2012). As shown in Fig. 4b,  
392 the mass fraction of aqSOA showed significant enhancement from less than 5% at  
393  $\text{ALWC} < 20 \mu\text{g m}^{-3}$  to 17–22% at  $\text{ALWC} > 60 \mu\text{g m}^{-3}$  with a corresponding decrease  
394 in OOA, although POA (BBOA+CCOA+HOA) and SOA (OOA+aqSOA)  
395 contributions were fairly constant across different ALWC levels (58–68% and  
396 32–42%). This result suggested a more intensive formation of aqSOA than OOA via  
397 aqueous-phase reactions, although aqSOA might be also formed from OOA,  
398 consistent with the recent research in northwest China (Zhao et al., 2019; Zhong et al.,  
399 2021). Additionally, the increasing  $f_{29}$  ( $\text{CHO}^+$ ) from 0.010 to 0.227 as a function of  
400 ALWC was observed during the campaign (Fig. 4b). The values of  $f_{29}$  significantly  
401 increased from 0.055 to 0.210 when ALWC increased from  $60 \mu\text{g m}^{-3}$  to  $100 \mu\text{g m}^{-3}$   
402 ( $p < 0.001$ ), consistent with OA mass concentrations (13.2–109.1  $\mu\text{g m}^{-3}$ ) during the  
403 campaign (Fig. 4b). According to the laboratory analysis of organic standards,  
404 previous research found that the spectra of standard organic species without alcohol  
405 group showed low  $f_{29}$  ( $< 0.05$ ), while high  $f_{29}$  values (0.05–0.15) were found for  
406 polyols and species with non-acid OH groups produced from biomass-burning  
407 emissions (Canagaratna et al., 2015; Gilardoni et al., 2016; Zhao et al., 2014). This  
408 further highlighted the potential formation of organic compounds with hydroxyl  
409 groups (i.e., glyoxal and methylglyoxal) under high ALWC conditions. Overall, these  
410 results pointed to the fact that the observed aqSOA could be formed from

411 biomass-burning emissions via aqueous-phase reactions, reinforcing the BBOA role in  
 412 increasing PM<sub>2.5</sub> mass concentration.



413  
 414 **Figure 3.** Scatter plot of the mass fraction of aqSOA in BC+NR-PM<sub>2.5</sub> versus ALWC colored by  
 415 the  $f_{29}$  (normalized mass spectrum signal at  $m/z$  29) during the campaign.  $f_{29}$  (mainly CHO<sup>+</sup>) is a  
 416 tracer for alcohol compounds and used to monitor the aqueous-phase oxidation of organic  
 417 compounds (i.e., glyoxal).



418  
 419 **Figure 4.** Variations of (a) OA factors mass concentrations, and (b) OA mass concentrations,  $f_{29}$  (a  
 420 tracer for alcohol compounds), and mass fraction of OA factors as a function of ALWC. The data

421 were grouped into different bins according to a  $10 \mu\text{g m}^{-3}$  increment of ALWC.

422 To identify the formation of aqSOA and its precursors under different  $\text{PM}_{2.5}$   
423 pollution levels, the relationship between aqSOA and BBOA or OOA mass  
424 concentrations with ion fragments tracers during CP and PP was performed,  
425 respectively. The correlation  $r^2$  between aqSOA and BBOA concentrations was  
426 higher during PP (0.64) than that during CP (0.54) ( $p < 0.001$ ) (Fig. 5a and c). Though  
427 aqSOA and BBOA concentrations increased with the increase of ALWC during CP  
428 and PP, the correlations between ALWC and aqSOA or BBOA concentrations were  
429 relatively stronger during PP than that during CP ( $p < 0.001$ ). Fig. 5b and d show that  
430  $f_{29}$  was highly correlated with aqSOA formation during CP and PP. A few data points  
431 with high aqSOA and OOA concentrations had low  $f_{29}$  values (0.071–0.102) in Fig. 5d,  
432 while the average value of  $f_{44}$  (normalized mass spectrum signal at  $m/z$  44) of these  
433 data points ( $0.103 \pm 0.024$ ) was 1.3 times that of all data points ( $0.080 \pm 0.035$ ) during  
434 PP. It was likely due to the formation of more-oxidized OOA under high ALWC  
435 values ( $> 80 \mu\text{g m}^{-3}$ ) in this study (Xu et al., 2017). Previous research found that the  
436  $f_{29}$  values of polyols and species with non-acid OH groups from biomass-burning  
437 emissions were lower than 0.15 (Canagaratna et al., 2015; Gilardoni et al., 2016; Zhao  
438 et al., 2014). Moreover, the mass fraction of aqSOA showed a stable increasing trend  
439 and remained high levels (from 18% to 22%) at  $\text{ALWC} > 80 \mu\text{g m}^{-3}$ , which was  
440 associated with a corresponding decrease in OOA (from 15% to 10%) (Fig. 4b).  
441 Compared with OOA ( $p > 0.1$ ), the aqSOA concentrations showed strong positive  
442 correlation with ALWC ( $r^2 = 0.73$ ,  $p < 0.001$ ) when  $\text{ALWC} > 80 \mu\text{g m}^{-3}$  during PP. In  
443 contrast, ALWC showed the weak correlations with aqSOA and OOA concentrations  
444 during CP ( $p > 0.1$ ). It should be noted that a strong anticorrelation between aqSOA  
445 and OOA concentrations was observed during PP at  $\text{ALWC} > 80 \mu\text{g m}^{-3}$  when  $f_{29} >$   
446  $0.15$  ( $r^2 = 0.76$ ,  $p < 0.001$ ), but not during CP ( $p > 0.1$ ) (Fig. 5b and d). These results  
447 indicated that the aqSOA formation was more intensive than OOA at high ALWC  
448 levels during PP.

449 Previous research demonstrated that  $f_{44}$  (representation of aged OA) could be  
450 used as a tracer of aged SOA,  $f_{43}$  (normalized mass spectrum signal at  $m/z$  43) as a

451 tracer of POA and fresh SOA, and  $f_{60}$  (presence of anhydrosugars) as a tracer of  
452 BBOA (Cubison et al., 2011; Ng et al., 2010). Additionally, m/z's 44 and 43 are  
453 usually from different functional groups and the ratio changes as a function of  
454 atmospheric aging. The triangle plot of  $f_{44}$  versus  $f_{43}$  has been widely used to  
455 characterize OA evolution, and  $f_{44}$  versus  $f_{60}$  is commonly used to investigate the  
456 aging trend of BBOA (Ortega et al., 2013; Paglione et al., 2020; Xu et al., 2017; Xu et  
457 al., 2019). As shown in Fig. 6, the bottom region of the triangle was dominated by  
458 BBOA, CCOA, and HOA with low  $f_{44}$  (0.040, 0.017, and 0.016, respectively) in this  
459 study, indicating that they were freshly emitted and less oxidized. However, the  $f_{44}$  of  
460 SOA factors (i.e., OOA and aqSOA) (0.118 and 0.117) were observably higher than  
461 POA factors, showing the freshly oxidized properties of SOA. Meanwhile,  $f_{44}$  of  
462 aqSOA was close to that observed in fogs (Gilardoni et al., 2016; Kim et al., 2019),  
463 highlighting the presence of aqueous-phase reactions in this study. The relative  
464 abundance of m/z 45 (mainly  $\text{HCO}_2^+$ ), a tracer ion for carboxylic acids, was higher in  
465 the aqSOA spectra than in the OOA spectrum (Fig. S9). It was consistent with previous  
466 research which found that aqueous-phase reactions were important sources of  
467 oxygenated organic compounds, including organic acids (Ervens et al., 2011; Kim et  
468 al., 2019; McNeill, 2015; Sun et al., 2010; Yu et al., 2014). Fig. 6b shows BBOA and  
469 aqSOA with higher  $f_{60}$  values (0.019 and 0.011) than CCOA (0.009) and HOA (0.008).  
470 The  $f_{60}$  value of OOA was 0.002, lower than the typical background value (0.003) in  
471 the atmosphere without biomass burning influence (Cubison et al., 2011). The mass  
472 spectrometry feature of aqSOA showed large  $f_{44}$  and  $f_{60}$  values, laying in a schematic  
473 space of aged BBOA based on mass spectrometry features in previous research  
474 (Cubison et al., 2011; Ortega et al., 2013). Additionally, BBOA contains abundant  
475 water-soluble organic compounds (WSOC) with (i.e., sugars, phenols, and organic  
476 acids), that can form aqSOA via efficient aqueous-phase reactions (i.e., oxidation and  
477 oligomerization reactions) (Ervens et al., 2011; Gilardoni et al., 2016; Lee et al., 2013;  
478 Lei et al., 2024; Li et al., 2020; Powelson et al., 2014). In contrast, OOA formation  
479 primarily relies on gas-phase oxidation of VOCs with high-reactivity (i.e., aromatics  
480 and long-chain alkanes) (i.e., OH radicals), which has low concentrations in BBOA

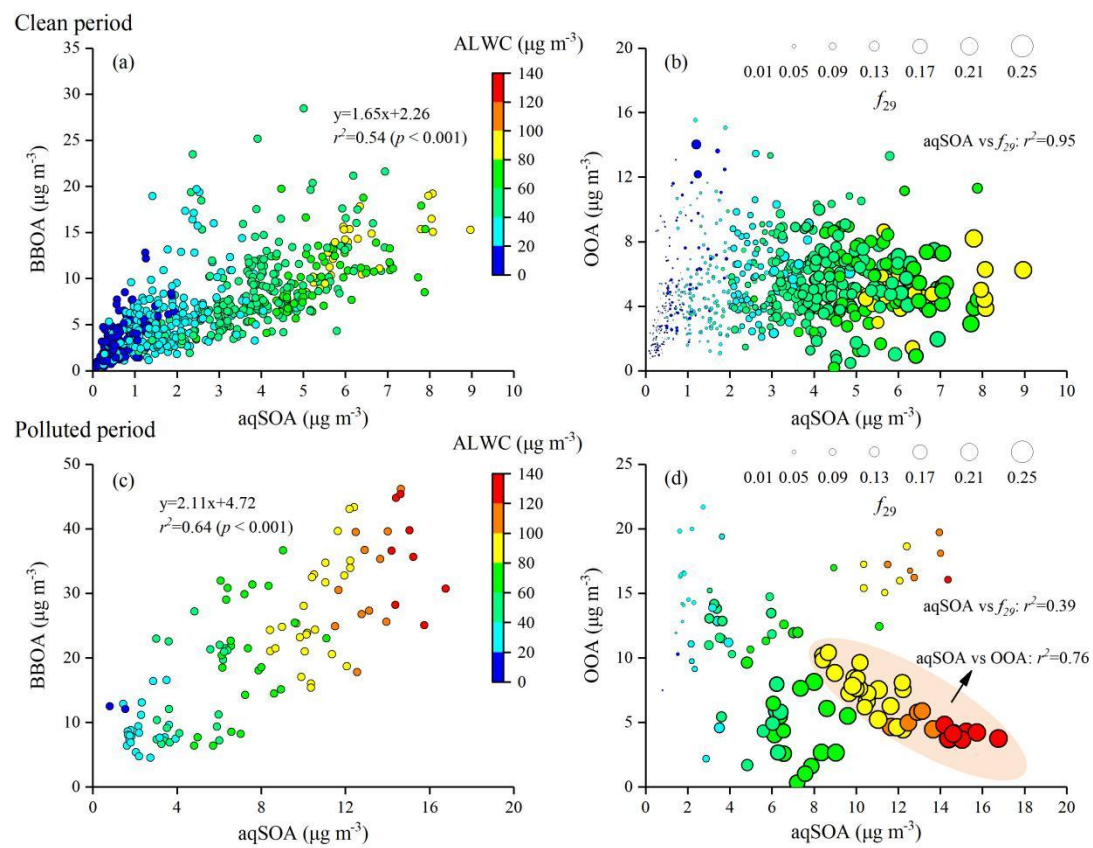
481 (Akagi et al., 2011; Jimenez et al., 2009; Shrivastava et al., 2017; Yokelson et al.,  
482 2007). This suggested that BBOA could be the important precursors for aqSOA  
483 instead of OOA via aqueous-phase reactions. These results were consistent with  
484 previous research and most of the observation data were within the triangle space  
485 (Bao et al., 2023; Kim et al., 2019; Paglione et al., 2020). It should be noted that these  
486 processes of aqSOA formation could be more intense and important during autumn  
487 due to elevated precursor concentrations (i.e., BBOA), ALWC, and RH values, though  
488 they are chemically robust and likely occur year-round.

489 During PP, the  $f_{44}$  values ranging from 0.022 to 0.140 ( $0.080 \pm 0.035$ ) were  
490 significantly higher than that during CP (0.021–0.150,  $0.064 \pm 0.019$ ) ( $p < 0.001$ ),  
491 while the  $f_{43}$  value was slightly lower with an average of  $0.062 \pm 0.027$ . Compared  
492 with CP ( $r^2 = 0.17$ , slope =  $-0.53$ ),  $f_{44}$  showed a more significant increase as the  
493 decreasing of  $f_{43}$  with higher  $r^2$  value (0.70) and the regression slope of  $f_{44}$  versus  $f_{43}$   
494 ( $-1.09$ ) was closer to  $-1$  during PP. This indicated that more aged SOA existed in the  
495 atmosphere during PP (Fig. 6a and c). It should be noted that the points of  $f_{44}$  versus  
496  $f_{43}$  were inside the upper boundary of the triangle region, and most points were  
497 outside the bottom boundary of the triangle region during PP. These results suggested  
498 that less oxidized SOA were formed via aqueous-phase reactions instead of  
499 photo-chemical reactions during PP (Kim et al., 2019; Zhao et al., 2019). Moreover,  
500 these points outside the bottom boundary of the triangle region with higher  $f_{44}$  ( $> 0.05$ )  
501 and lower  $f_{43}$  ( $< 0.06$ ) showed relatively higher ALWC during PP, but not during CP.

502 Here, the triangle plots of  $f_{44}$  versus  $f_{60}$  colored by ALWC under different PM<sub>2.5</sub>  
503 pollution levels were analyzed (Fig. 6b and d), when the link between aqSOA and  
504 BBOA was further stressed by a schematic representation of aged BBOA. Except for  
505 several points, the  $f_{60}$  values were ubiquitously higher than 0.003, and most points fell  
506 in the triangular region, suggesting the contribution of biomass burning to OA. During  
507 PP, the  $f_{60}$  values ranging from 0.005 to 0.019 ( $0.010 \pm 0.004$ ) were similar with CP  
508 (from 0.004 to 0.019,  $0.010 \pm 0.003$ ). The correlation  $r^2$  between  $f_{44}$  and  $f_{60}$  was higher  
509 during PP (0.72) than that during CP (0.31) ( $p < 0.001$ ). Moreover, compared with all  
510 data points during PP, those in the schematic space of aged BBOA showed relatively

511 higher ALWC, a pattern that differed from observations during CP.

512 Regional transport significantly influences the aging of BBOA in the SCB.  
513 Previous studies have demonstrated that the northeast winds prevail during autumn in  
514 the SCB and facilitate the transport of pollutants along the Dazhou → Guang'an →  
515 Hechuan pathway, and this northeast-southwest transport pathway had a significant  
516 impact on Chongqing (Peng et al., 2019; Wang et al., 2018). As shown in Fig. S11, air  
517 masses predominantly originated from northeastern Chongqing, which is an area with  
518 widespread agricultural burning activities (He et al., 2015; Luo et al., 2020), and were  
519 transported over short ranges during the campaign. Compared to other air mass  
520 clusters, the highest contribution and concentration of BBOA in total PM<sub>2.5</sub> were  
521 observed when air masses passed through northeastern Chongqing. The percentage of  
522 air mass trajectories that passed through biomass-burning-influenced regions was  
523 higher during PP (~57%) than CP (~35%). Unlike cluster 3 during CP, air masses  
524 originating from northeastern Chongqing (cluster 2) during PP showed significantly  
525 higher contributions and concentrations of BBOA (24.7%, 27.8 μg m<sup>-3</sup>) and aqSOA  
526 (9.4%, 10.6 μg m<sup>-3</sup>) than other clusters ( $p < 0.001$ ). In addition, cluster 2 exhibited  
527 notably higher values of ALWC (93.7 μg m<sup>-3</sup>), Abs<sub>370,BrC,sec</sub> (105.1 Mm<sup>-1</sup>),  $f_{44}$  (0.113),  
528 and the NO<sub>3</sub>/SO<sub>4</sub> ratio (2.1, a tracer for BBOA aging (Liu et al., 2024; Zhang et al.,  
529 2025)) than other clusters during PP ( $p < 0.001$ ). During PP, approximately 68% of  
530 the trajectories in cluster 2 passed through biomass-burning-influenced regions, with  
531 transport times to the sampling site ranging between 12 and 48 hours. This time frame  
532 is consistent with previous research on the aqueous-phase aging process of biomass  
533 burning emissions (Cubison et al., 2011; Hennigan et al., 2010; Ortega et al., 2013;  
534 Zhu et al., 2023). These results suggested that regional transport of BBOA primarily  
535 originated from northeastern Chongqing, and aged to aqSOA within approximately 12  
536 to 48 hours.

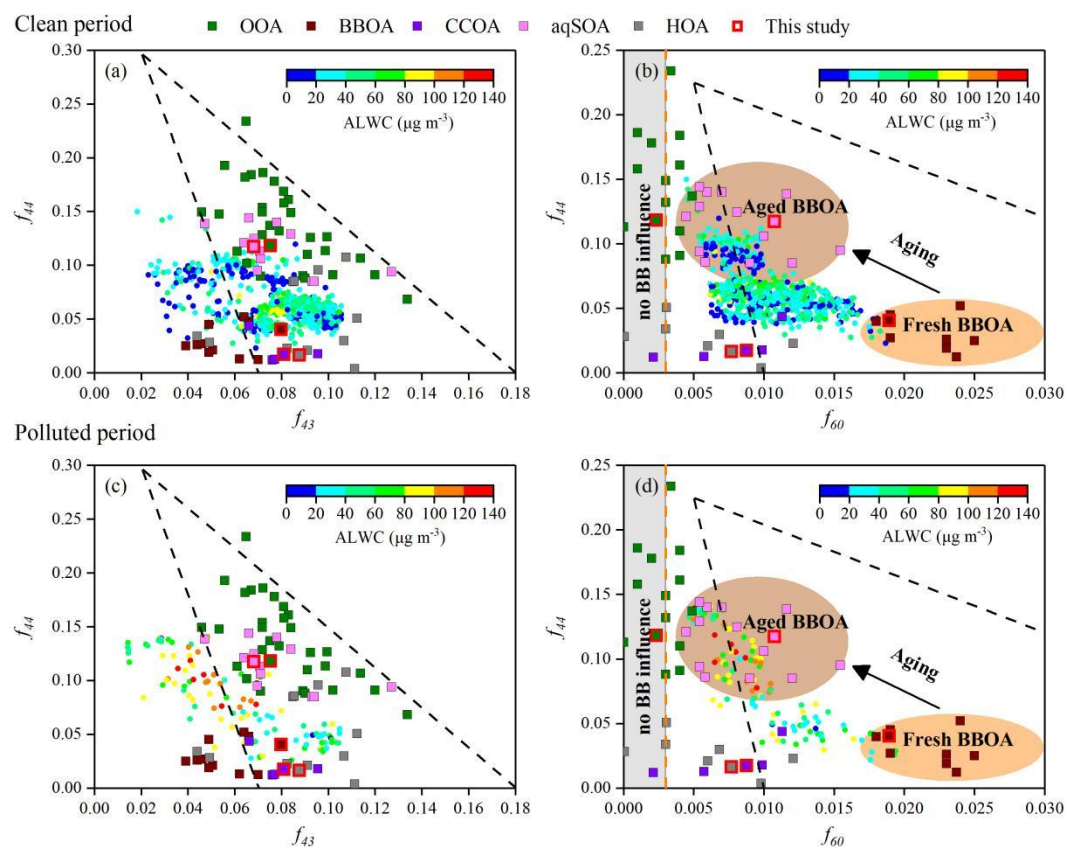


537

538 **Figure 5.** Scatter plots of aqSOA versus (a, b) BBOA and (c, d) OOA mass concentrations

539 colored by ALWC during clean period and polluted period. The size of the symbols in (b) and (d)

540 increases with the increase of the  $f_{29}$  value, which is a tracer for alcohol compounds.



541

542 **Figure 6.** Triangle plots of **(a, c)**  $f_{44}$  (normalized mass spectrum signal at  $m/z$  44) versus  $f_{43}$   
543 (normalized mass spectrum signal at  $m/z$  43), and **(b, d)**  $f_{44}$  versus  $f_{60}$  (normalized mass spectrum  
544 signal at  $m/z$  60) colored by ALWC (circles) during clean period and polluted period. The dashed  
545 lines in **(a)** and **(c)** were derived from Ng et al. (2010) and used to follow the aging of OA  
546 components in the atmosphere. The background space ( $f_{60} < 0.003$ ) without biomass burning  
547 influence was also shown by the grey shaded area. The background value of secondary aged OA  
548 (brown dashed line) and the black dashed lines characterising the aging of BBOA in **(b)** and **(d)**  
549 were derived from Cubison et al. (2011). The data points (squares) included the measurements in  
550 this study (bordered in red) and previous research (Bao et al., 2023; Gilardoni et al., 2016; Kim et  
551 al., 2019; Ng et al., 2011a; Paglione et al., 2020; Xu et al., 2015; Xu et al., 2017; Xu et al., 2019;  
552 Zhao et al., 2017; Zhao et al., 2019).  $f_{43}$  (mainly  $\text{C}_2\text{H}_3\text{O}^+$ ) is a tracer for POA and fresh SOA.  $f_{44}$  is  
553 a proxy of the OA oxygenation degree and used as a tracer for aged SOA.  $f_{60}$  is a proxy of  
554 anhydrosugars emitted from biomass burning.

### 555 3.3 Evolution of BrC Absorption

556 Previous research indicated that OA from fresh and aged biomass-burning  
557 emissions, which exhibited absorption properties across UV to Vis range with  
558 significantly higher AAE value than BC, might contribute to a net positive radiative  
559 forcing (Laskin et al., 2015). Therefore, the BrC absorption properties and their  
560 relationship with five OA factors were analyzed in this study. The values of  $Abs_{\lambda,BrC,pri}$   
561 and  $Abs_{\lambda,BrC,sec}$  were obtained by MRS method, and the MLR method was used to  
562 estimate Abs of five OA factors at each wavelength (SI Text S3 and S4). The average  
563 value of  $Abs_{370,BrC}$  was  $42.4 \pm 28.5 \text{ Mm}^{-1}$  (accounting for 49.2% of  $Abs_{370}$ ), much  
564 higher than  $Abs_{660,BrC}$  ( $2.6 \pm 1.3 \text{ Mm}^{-1}$ , 10.5%), suggesting a high absorption  
565 efficiency for BrC in the near-UV wavelength. The  $Abs_{\lambda,BrC,pri}$  and  $Abs_{\lambda,BrC,sec}$   
566 accounted for 56.8%–72.5% and 27.5%–43.2% of  $Abs_{\lambda,BrC}$  from 370 nm to 660 nm  
567 respectively, indicating primary emissions were the main contributors to BrC  
568 absorption (Fig. S13). However, the contribution of  $Abs_{\lambda,BrC,sec}$  to  $Abs_{\lambda,BrC}$  increased  
569 with wavelength, suggesting the impact on  $Abs_{BrC}$  from SOA should not be ignored.  
570 Hereafter, we show that aqSOA formation from aged BBOA contributed to the BrC  
571 budget and was strong absorption across UV to Vis range.

572 The data at 370 nm with higher signal-to-noise ratios and  $Abs_{BrC}$  contribution  
573 was chosen to further analyze the correlations of BrC absorption with various OA  
574 components. As described in section 2.3.3, the Abs of five OA factors at each  
575 wavelength were obtained by the MLR method (Table S1). Compared with CCOA  
576 ( $Abs_{370,CCOA}$ ), HOA ( $Abs_{370,HOA}$ ), and OOA ( $Abs_{370,OOA}$ ) (11.5%, 9.1%, and 11.1%),  
577 the Abs at 370 nm calculated for BBOA ( $Abs_{370,BBOA}$ ) and aqSOA ( $Abs_{370,aqSOA}$ )  
578 showed higher contributions (51.9% and 16.4%) to  $Abs_{370,BrC}$ , consistent with the  
579 higher MAC values (Fig. S15). Fig. S16 presents the correlations between  $Abs_{370,BrC}$   
580 and the mass concentrations of OOA, BBOA, CCOA, aqSOA, HOA, and m/z 60.  
581  $Abs_{370,BrC}$  showed the strongest positive correlations with BBOA and m/z 60 (ion  
582 fragments tracers of BBOA) concentrations ( $r^2 = 0.77$ ,  $p < 0.001$ ), followed by  
583 aqSOA concentrations ( $r^2 = 0.69$ ,  $p < 0.001$ ). In contrast, the correlations with HOA

删除[臻予珍愿]: 12

删除[臻予珍愿]: 14

删除[臻予珍愿]: 15

584 concentrations ( $r^2 = 0.36$ ), CCOA ( $r^2 = 0.25$ ), and OOA ( $r^2 = 0.09$ ,  $p > 0.1$ ) were  
585 much weaker. Compared with other OA factors (except BBOA), the contribution of  
586 Abs<sub>370,aqSOA</sub> to Abs<sub>370,BrC</sub> was relatively higher (Table S1), when the correlation  
587 between Abs<sub>370,BrC</sub> and aqSOA concentrations was also stronger. These results might  
588 be related to the aqSOA formed from the aged BBOA via aqueous-phase reactions.  
589 Gilardoni et al. (2016) demonstrated that aqSOA formation from aged BBOA via  
590 aqueous-phase reactions in the ambient atmosphere contributed to the BrC budget and  
591 exhibited slightly higher AAE<sub>467-660</sub> (AAE of aerosols from 467 nm to 660 nm )  
592 values than the fresh and processed biomass-burning emissions in laboratory  
593 experiments. The MAC values of the five resolved OA components equivalent to the  
594 a–e values in the MLR method at different wavelengths were shown in Fig. S15.  
595 Among these, BBOA showed the highest MAC value (2.37 m<sup>2</sup> g<sup>-1</sup>), followed by  
596 aqSOA (1.23 m<sup>2</sup> g<sup>-1</sup>) at 370 nm, indicating that the oxidation of BBOA to aqSOA  
597 decreased light absorption at short wavelengths. Previous research found that the  
598 MAC of BBOA at 365 nm was twice that of SOA, which was associated with the  
599 water-soluble BrC (Lorenzo et al., 2017; Washenfelder et al., 2015). The AAE values  
600 of OA factors, calculated by a power-law fitting of Abs for these OA factors from 370  
601 nm to 660 nm (Qin et al., 2018; Wang et al., 2019b), were shown in Fig. S15. It  
602 should be noted that aqSOA had the lowest AAE<sub>370-660,aqSOA</sub> value (3.54), while  
603 BBOA has the highest AAE<sub>370-660,BBOA</sub> value (4.93). Moreover, the contribution of  
604 aqSOA to Abs<sub>BrC</sub> increased from 16.4% to 26.7% from 370 to 660 nm, while the  
605 contribution from BBOA decreased from 51.9% to 39.1% from 370 to 660 nm. These  
606 suggested aqSOA formation from aged BBOA might play an important role in the  
607 light absorption of BrC across UV to Vis range.

608 Fig. 7 shows the ternary contour map to quantify the contribution of BBOA,  
609 CCOA, and HOA factors to Abs<sub>370,BrC,pri</sub>, when the strong positive correlation ( $p <$   
610 0.001) and high slope of the linear regression (1.80) between BBOA mass  
611 concentrations and Abs<sub>370,BrC,pri</sub> were observed. Among these POA factors, the high  
612 mass fractions of BBOA to POA were consistent with the high Abs<sub>370,BrC,pri</sub> values  
613 (Fig. 7a). For example, the most data of Abs<sub>370,BrC,pri</sub> higher than 49.1 Mm<sup>-1</sup> (90th

删除[臻予珍愿]: 14

删除[臻予珍愿]: 14

614 percentile of  $Abs_{370,BrC}$ ) fell in the region of high BBOA/POA values ( $> 0.5$ ).  
615 Moreover,  $Abs_{370,BrC,pri}$  significantly increased with the increases of BBOA and m/z 60  
616 mass concentrations with higher  $r^2$  values (0.63 and 0.55) than HOA and CCOA (0.19  
617 and 0.14) (Fig. 7b). These results indicated the major contribution of BBOA to  
618 primary BrC light absorption.

619 During the campaign, the relationship between  $Abs_{370,BrC,sec}$  and SOA factors  
620 mass concentrations was analyzed to understand the correlation between secondary  
621 BrC absorption and its chromophores. As shown in Fig. S17,  $Abs_{370,BrC,sec}$  significantly  
622 increased with the increase of aqSOA concentrations ( $r^2 = 0.44$ ,  $p < 0.001$ ) and high  
623  $Abs_{370,BrC,sec}$  values were consistent with the high ALWC values, this was not the case  
624 for OOA ( $p > 0.1$ ). The slope of the linear regression (3.50) between aqSOA mass  
625 concentrations and  $Abs_{370,BrC,sec}$  was higher than OOA (Fig. S17), so was the MAC  
626 values of aqSOA across UV to Vis range (Fig. S15). To further characterize the  
627 evolution of secondary BrC absorption,  $Abs_{370,BrC,sec}$  was normalized by  $\Delta CO$  (the  
628 background-corrected CO mixing ratios) to minimize the effect of boundary layer  
629 height (Fig. 8) (DeCarlo et al., 2010). Here, the background CO value (400 ppb) was  
630 defined as the lowest 1.25th percentile of the CO values during the campaign (Kondo  
631 et al., 2006). Fig. 8 shows that the values of  $Abs_{370,BrC,sec}/\Delta CO$  increased with the  
632 increases of aqSOA and ALWC concentrations from 17:00 to 03:00 LT ( $r^2 = 0.63$ ,  
633  $0.57$ ,  $p < 0.001$ ), while  $Abs_{370,BrC,pri}/\Delta CO$  slightly decreased with the increases of  
634 BBOA and m/z 60 concentrations ( $r^2 = 0.35$ ,  $0.33$ ,  $p < 0.001$ ). Additionally, the mass  
635 concentrations of  $NO_3$ ,  $NH_4$ , and  $NO_2$  from 17:00 to 03:00 LT were 1.2, 1.2, and 1.3  
636 times that from 04:00 to 16:00 LT during the campaign. These results were similar to  
637 those observed in SCB during winter (Peng et al., 2025; Wu et al., 2024). As  
638 described in section 3.2, the SOA with hydroxyl groups (i.e., glyoxal and  
639 methylglyoxal) could be formed from the aged BBOA via aqueous-phase reactions  
640 under high ALWC during the campaign. Previous research have shown that oligomers  
641 (involving two glyoxal molecules) formed via aqueous reactions of glyoxal with  $NH_3$   
642 contain C=C or C=N bonds, exhibiting strong absorption at near-UV (Laskin et al.,  
643 2015; Lee et al., 2013; Nozière et al., 2009; Powelson et al., 2014). This suggested

删除[臻予珍愿]: 16

删除[臻予珍愿]: 16

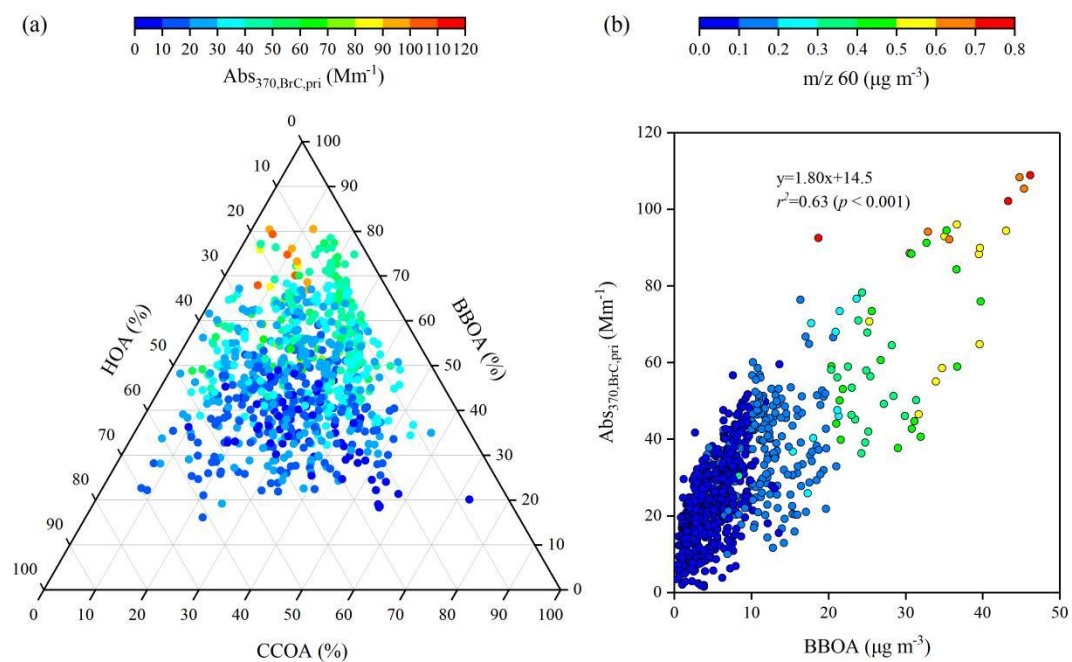
删除[臻予珍愿]: 14

644 secondary BrC chromophores with strong absorption at 370 nm were formed under  
645 the high ALWC from 17:00 to 03:00 LT, which might be related to the aqSOA from  
646 the aged BBOA via aqueous-phase reactions. The low values of  $Abs_{370,BrC,sec}/\Delta CO$  at  
647 12:00–14:00 LT could be related to the photolysis and/or photooxidation causing BrC  
648 photobleaching (Sareen et al., 2013; Zhao et al., 2015). Overall, we suggested that  
649 aqSOA formed from biomass-burning emissions might be important for BrC  
650 absorption, especially at night during the campaign.

651 Previous studies also provided evidence that spring may experience similar but  
652 less intense biomass-burning activity (Chen et al., 2014; Chen et al., 2017; Tao et al.,  
653 2014), with comparable aqueous chemistry though potentially increased  
654 photochemical bleaching of BrC (Wang et al., 2019a). Though winter features lower  
655 biomass-burning emissions, secondary BrC likely formed from BBOA through  
656 aqueous-phase reactions under high  $NO_x$  and  $NH_4$  concentrations and stagnant  
657 conditions after sunset during winter in SCB (Peng et al., 2025; Wu et al., 2024).  
658 Elevated temperature and  $O_x$  ( $O_x = NO_2 + O_3$ ) levels could enhance photochemical  
659 oxidation for secondary BrC formation during summer, while also promoting BrC  
660 photobleaching (Wu et al., 2024). It should be noted that the seasonal  
661 biomass-burning emissions and associated chemical processing of carbonaceous  
662 aerosols must be accounted for in climate and air quality models. This is critical to  
663 avoid underestimating aerosol impacts in autumn and overestimating them in other  
664 seasons. In general, the research of BrC chromophores is still in the early stage, and  
665 more studies of the quantitative link between the chemical composition and light  
666 absorption properties of BrC chromophores and biomass-burning emissions during  
667 different season are necessary to better understand.

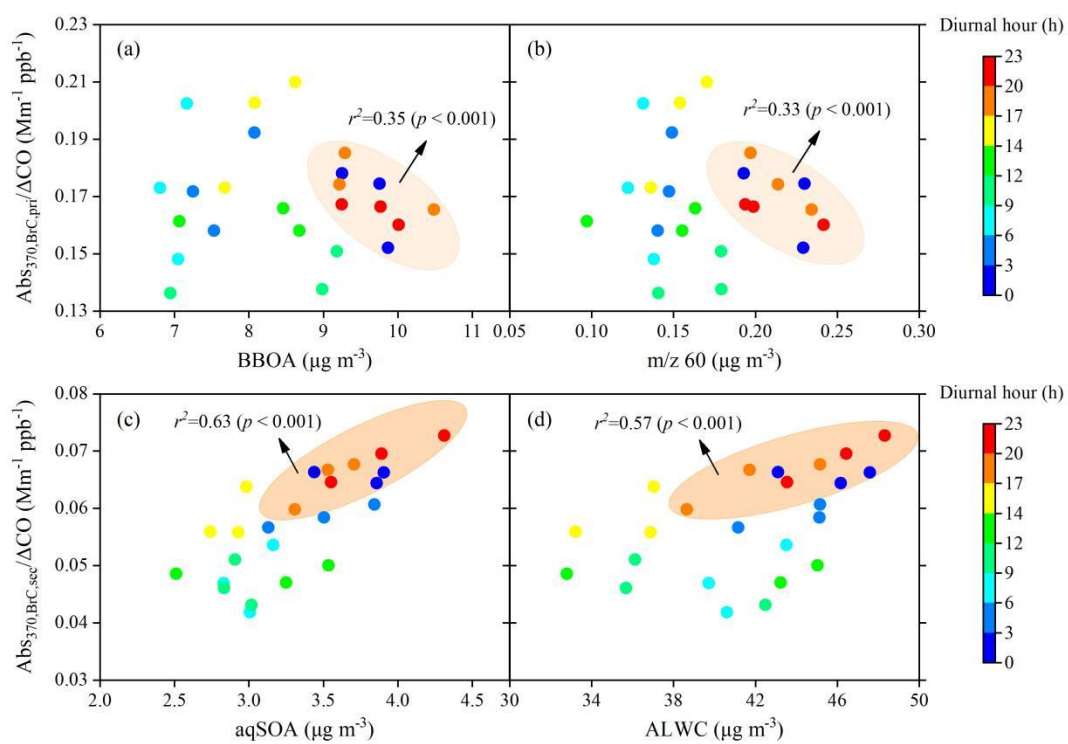
668  $AAE_{370-880}$  was another key parameter to characterize the absorption properties  
669 of aerosols, its correlations with the mass fraction of aqSOA ( $f_{aqSOA}$ ) and BBOA  
670 ( $f_{BBOA}$ ) to OA, and BC-to-OA ratios were shown in Fig. 9. During the campaign, the  
671 strong positive correlation ( $r^2 = 0.49$ ,  $p < 0.001$ ) between  $AAE_{370-880}$  and  $f_{aqSOA}$  was  
672 observed with  $AAE_{370-880}$  values up to 2.65, while  $AAE_{370-880}$  values increased with  
673 the slight increase of  $f_{BBOA}$  in general ( $r^2 = 0.21$ ,  $p < 0.001$ ) (Fig. 9a and c). AAE was

674 calculated using a power-law fitting of aerosol absorption values (Qin et al., 2018;  
675 Wang et al., 2019**b**). While BC concentration is linearly dependent on Abs<sub>BC</sub>, OA  
676 concentration does not follow the same pattern with Abs<sub>BC</sub>. The mixing state of BC  
677 and OA, influenced by combustion conditions, can also affect AAE. Previous studies  
678 have shown that biomass-burning emissions can impact absorption properties, which  
679 is reflected in the relationship between AAE and the BC-to-OA ratio (a measure of the  
680 combustion conditions) (Lu et al., 2015; Saleh et al., 2014). Thus, the relationship  
681 observed in Fig. 9b reflected the influence of biomass-burning emissions during the  
682 campaign, and the parameterized curve in this study (black) was consistent with prior  
683 research (red) using wavelengths from 370 nm to 880 nm (Lu et al., 2015). Here, 950  
684 nm and 880 nm were used as the highest wavelength respectively, and similar values  
685 were found between AAE<sub>370-950</sub> and AAE<sub>370-880</sub> (within 10.0%). It should be noted  
686 that the data points of high AAE<sub>370-880</sub> were consistent with the low BC-to-OA ratios  
687 and large  $f_{\text{aqSOA}}$  values in general. Moreover, the average value of AAE<sub>370-880</sub> observed  
688 in this study (1.95) was higher than AAE<sub>370-950</sub> observed in the laboratory experiments  
689 of fresh and photo-chemically aged biomass-burning emissions (i.e., 1.38 and 1.48 for  
690 fresh oak and pocosin pine, 1.42 and 1.73 for aged oak and pocosin pine) (Saleh et al.,  
691 2013).



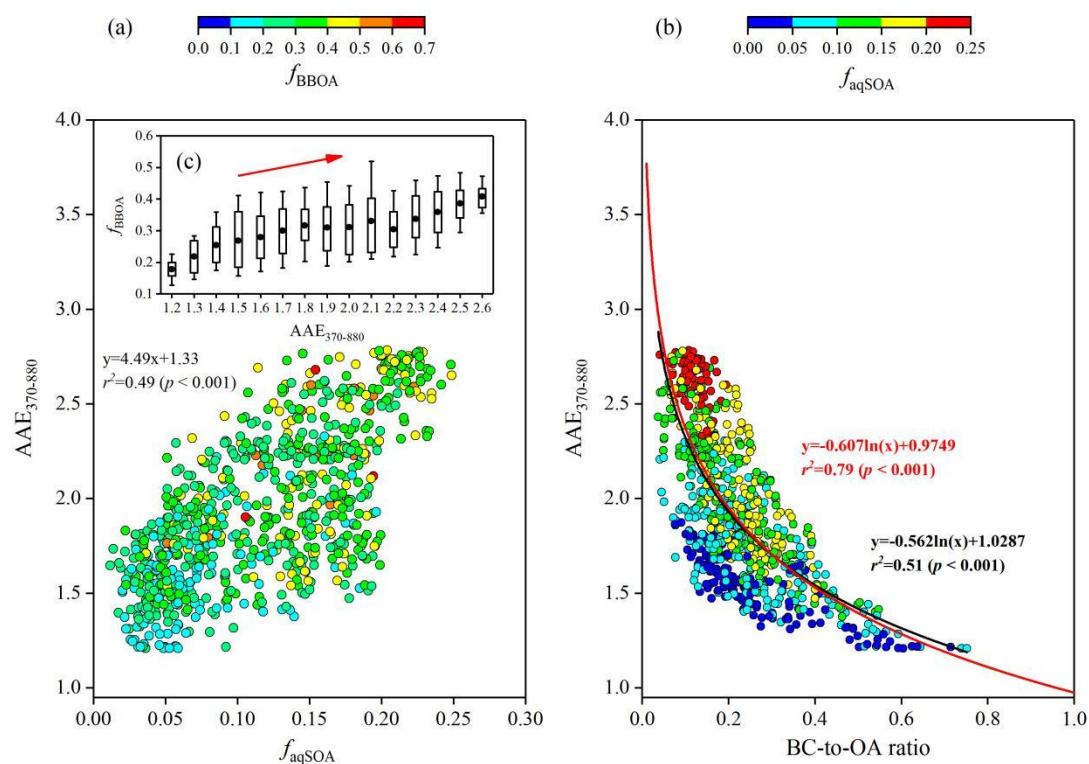
692

693 **Figure 7. (a)** Ternary diagram for the mass fractions of BBOA, CCOA, and HOA in POA colored  
 694 by Abs<sub>370,BrC,pri</sub>, and **(b)** scatter plot of BBOA mass concentrations versus Abs<sub>370,BrC,pri</sub> colored by  
 695 m/z 60 mass concentrations.



696

697 **Figure 8.** Scatter plots of  $\text{Abs}_{370,\text{BrC,pri}}/\Delta\text{CO}$  versus **(a, b)** BBOA and  $m/z$  60 mass concentrations  
 698 and  $\text{Abs}_{370,\text{BrC,sec}}/\Delta\text{CO}$  versus **(c, d)** aqSOA and ALWC colored by the local time.



699  
 700 **Figure 9.** Relationship between **(a)**  $\text{AAE}_{370-880}$  and the mass fraction of aqSOA ( $f_{\text{aqSOA}} =$   
 701  $\text{aqSOA/OA}$ ) colored by the mass fraction of BBOA ( $f_{\text{BBOA}} = \text{BBOA/OA}$ ), and **(b)** BC-to-OA ratios  
 702 colored by  $f_{\text{aqSOA}}$ . **(c)** Variations of  $f_{\text{BBOA}}$  as a function of  $\text{AAE}_{370-880}$ . The red curve in **(b)** was the  
 703 best fit curve to data taken from Lu et al. (2015) and described the Abs of fresh and aged BBOA.

#### 704 4 Conclusions

705 This study conducted comprehensive real-time measurements of the light  
 706 absorption properties and chemical composition of carbonaceous aerosols during  
 707 autumn in the Sichuan Basin, China. The findings provided direct ambient evidence  
 708 demonstrating that aqueous secondary organic aerosol (aqSOA) formed from the aged  
 709 biomass-burning emissions under high aerosol liquid water content ( $\text{ALWC} > 60 \mu\text{g}$   
 710  $\text{m}^{-3}$ ) conditions significantly contributes to both aerosol pollution and light absorption.  
 711 Organic aerosol (OA) was identified as the dominant component of  $\text{PM}_{2.5}$  ( $46.6 \pm$

712 10.7%) and exhibited strong absorption properties at UV wavelengths ( $Ab_{S370,BrC} =$   
713  $42.4 \pm 28.5 \text{ Mm}^{-1}$ ). During pollution periods (PP), the average contribution and  
714 concentration of aqSOA to OA were 14.1% and  $7.6 \mu\text{g m}^{-3}$ , exhibiting enhanced  
715 oxidation ( $f_{29} = 0.141 \pm 0.062$ ,  $f_{44} = 0.080 \pm 0.035$ ) and substantial light absorption  
716 characteristics of OA ( $Ab_{S370,BrC} = 91.6 \text{ Mm}^{-1}$ ,  $AAE_{370-880} = 2.1$ ). Additionally, the  
717 less oxidized aqSOA formation via aqueous-phase reactions instead of  
718 photo-chemical reactions played a key role in the haze pollution dynamic evolution  
719 during PP. Furthermore, backward trajectory analysis revealed regional transport of  
720 BBOA primarily originated from northeastern Chongqing, and aged to aqSOA within  
721 approximately 12 to 48 hours. These results underscore that aqueous-phase reactions  
722 of BBOA—particularly during the transport of biomass-burning emissions—converts  
723 primary emissions into strong light-absorbing aqSOA, substantially influencing  
724 regional haze formation and radiative effects.

725 Our findings align with previous laboratory studies on biomass-burning BrC  
726 formation (Lu et al., 2015; Powelson et al., 2014), while providing novel ambient  
727 quantification of these processes under realistic atmospheric conditions. The  
728 parameterized curve of  $AAE_{370-880}$  versus BC-to-OA ratios in this study was  
729 consistent with the previous laboratory research on biomass-burning emissions. The  
730  $AAE_{370-880}$  values observed in this study (average = 1.95) were higher than those in  
731 the laboratory experiments of fresh and photo-chemically aged biomass-burning  
732 emissions (Saleh et al., 2013), and significantly increased with the increase of  $f_{aqSOA}$   
733 ( $r^2 = 0.49$ ,  $p < 0.001$ ). Additionally, the elevated  $Ab_{S370,BrC,sec}$  values were consistent  
734 with the high ALWC,  $NO_3$ , and  $NH_4$  values, and significantly increased with the  
735 increase of aqSOA concentrations ( $r^2 = 0.44$ ,  $p < 0.001$ ). These results suggest that  
736 aqueous-phase reactions of BBOA in high- $NO_x$  and high- $NH_4$  conditions produce  
737 secondary BrC with particularly strong light absorption. The campaign was conducted  
738 during autumn, which features intensive biomass-burning activity, and thus may not  
739 fully represent aerosol processes in other seasons. The relative uncertainty range of  
740  $Ab_{SBrC}$  was  $[-112\%, +42\%]$  at 370 nm due to the choice of  $AAE_{BC}$ . Our results  
741 underscore the importance of aqueous-phase processing in transforming

742 biomass-burning emissions, with important implications for climate and air quality  
743 modeling. The significant contribution of aqSOA to both aerosol mass and light  
744 absorption highlights the need for improved representation of aqueous processes in  
745 models. The linkages between aging timescales, transport pathways, and aqSOA  
746 formation in this study provide a transferable framework for understanding aqSOA  
747 processing in other humid regions influenced by biomass burning. Future research  
748 should prioritize molecular-level characterization of aqSOA precursors and products,  
749 quantification of aqueous reaction rates under ambient conditions, and multi-scale  
750 modeling to assess regional climate impacts. This study highlights that aqueous  
751 processes play an important role in the evolution of biomass-burning emissions and  
752 should be adequately considered in both air quality budgets and climate forcing  
753 balance on a global scale.

754

755 **Data availability.** The data generated and analysed in this study are available from  
756 <https://doi.org/10.5281/zenodo.14626304> (Peng et al., 2025).

757

758 **Author contributions.** CZ, CP, YD, and ZL designed the experiments. Data analysis  
759 and interpretation were performed by CP, ZT, HT, KZ, ZL, and GS. CP, XY, and MT  
760 wrote the paper. ZT, YC, XL, LZ, YC, and YF contributed to the paper with useful  
761 scientific discussions or comments.

762

763 **Competing interests.** The authors declare that they have no conflict of interest.

764

765 **Acknowledgements.** This study was supported by the National Natural Science  
766 Foundation of China (No. 42305126), National Key Research and Development  
767 Program of China (No. 2023YFC3709301), Natural Science Foundation of  
768 Chongqing Municipality (No. CSTB2022NSCQ-MSX0504).

删除[臻予珍愿]: Field observations indicated that secondary organic aerosol (SOA) accounts for most of organic aerosol (OA) worldwide and aqueous-phase oxidation is an important pathway for the SOA formation. Our results demonstrated the fact that aqSOA was originated from the aged biomass-burning emissions via aqueous-phase reactions under high ALWC in the ambient atmosphere. Additionally, the less oxidized aqSOA formation via aqueous-phase reactions instead of photo-chemical reactions played a key role in the haze pollution dynamic evolution during the polluted period. This study also indicated that the impact on secondary BrC absorption should not be ignored, although primary BrC dominated the BrC absorption across ultraviolet to visible range. The aqSOA formed from aged biomass-burning emissions significantly contributed to the BrC budget and showed stronger absorption across ultraviolet to visible range than other OA components (except BBOA). The similarity between ambient data and the parameterized curve of  $AAE_{370-880}$  versus BC-to-OA ratios in this study was consistent with the previous laboratory research on biomass-burning emissions. Higher values of  $AAE_{370-880}$  and  $MAC_{\lambda, aqSOA}$  reinforced that aqSOA formation from aged biomass-burning emissions via aqueous-phase reactions had stronger absorption than that via photo-chemically reactions. In conclusion, our results revealed the aqSOA formation and brownness from aged BBOA via aqueous-phase reactions and highlighted the importance of aqSOA on aerosol pollution and absorption in the Sichuan Basin, China. Brown aqSOA originating from biomass-burning emissions was an important player in air quality budget and climate forcing balance worldwide. And it should be taken into account in air quality and climate models for a correct description of the global OA budget and its climate-relevant optical properties. This study was helpful in understanding the formation, light properties, and impacts of aqSOA in the ambient atmosphere. Future research should focus on the molecular-level characterization, transportation, and reactivities of gas and particle-phase aqSOA precursors to improve understanding of aqSOA formation processes and absorption properties.

769 **References**

- 770 Akagi, S. K., Yokelson, R. J., Wiedinmyer, C., Alvarado, M. J., Reid, J. S., Karl, T.,  
771 Crouse, J. D., and Wennberg, P. O.: Emission factors for open and domestic  
772 biomass burning for use in atmospheric models, *Atmos. Chem. Phys.*, 11,  
773 4039–4072, <https://doi.org/10.5194/acp-11-4039-2011>, 2011.
- 774 Alfara, M. R., Prévôt, A. S. H., Szidat, S., Sandradewi, J., Sandradewi, S., Lanz, V.  
775 A., Schreiber, D., Mohr, M., and Baltensperger, U.: Identification of the Mass  
776 Spectral Signature of Organic Aerosols from Wood Burning Emissions, *Environ.*  
777 *Sci. Technol.*, 41, 5770–5777, <https://doi.org/10.1021/es062289b>, 2007.
- 778 Bahreini, R., Ervens, B., Middlebrook, A. M., Warneke, C., de Gouw, J. A., DeCarlo,  
779 P. F., Jimenez, J. L., Brock, C. A., Neuman, J. A., Ryerson, T. B., Stark, H.,  
780 Atlas, E., Brioude, J., Fried, A., Holloway, J. S., Peischl, J., Richter, D., Walega,  
781 J., Weibring, P., Wollny, A. G., and Fehsenfeld, F. C.: Organic Aerosol Formation  
782 in Urban and Industrial Plumes Near Houston and Dallas, Texas, *J. Geophys. Res.:*  
783 *Atmos.*, 114, D00F16, doi:10.1029/2008JD011493, 2009.
- 784 Bao, Z. E., Liu, Y. L., Meng, L. S., Han, Y., Tian, M., Shi, G. M., Wang, Q. Y., Huang,  
785 Y., Peng, C., Luo, B., Zhang, W., Wang, H. B., Cao, J. J., Yang, F. M., and Chen, Y.:  
786 Evaluating the effects of biomass burning on severe haze formation in a megacity  
787 of Sichuan Basin, Southwestern China, *J. Geophys. Res.:* *Atmos.*, 130,  
788 e2024JD042516, <https://doi.org/10.1029/2024JD042516>, 2025.
- 789 Bao, Z. E., Zeng, X. L., Zhou, J. W., Yang, F. M., Lu, K. D., Zhai, C. Z., Li, X., Feng,  
790 M., Tan, Q. W., and Chen, Y.: Evolution of black carbon and brown carbon during  
791 summertime in Southwestern China: An assessment of control measures during the  
792 2023 Chengdu Summer World University Games, *Environ. Pollut.*, 357, 124467,  
793 <https://doi.org/10.1016/j.envpol.2024.124467>, 2024.
- 794 Bao, Z. E., Zhang, X. Y., Li, Q., Zhou, J. W., Shi, G. M., Zhou, L., Yang, F. M., Xie, S.  
795 D., Zhang, D., Zhai, C. Z., Li, Z. L., Peng, C., and Chen, Y.: Measurement report:  
796 Intensive biomass burning emissions and rapid nitrate formation drive severe haze  
797 formation in the Sichuan Basin, China – insights from aerosol mass spectrometry,  
798 *Atmos. Chem. Phys.*, 23, 1147–1167, <https://doi.org/10.5194/acp-23-1147-2023>,

799 2023.

800 Canagaratna, M. R., Jayne, J. T., Jimenez, J. L., Allan, J. D., Alfarra, M. R., Zhang, Q.,  
801 Onasch, T. B., Drewnick, F., Coe, H., Middlebrook, A., Delia, A., Williams, L. R.,  
802 Trimborn, A. M., Northway, M. J., DeCarlo, P. F., Kolb, C. E., Davidovits, P., and  
803 Worsnop, D. R.: Chemical and microphysical characterization of ambient aerosols  
804 with the aerodyne aerosol mass spectrometer, *Mass Spectrom. Rev.*, 26, 185–222,  
805 <https://doi.org/10.1002/mas.20115>, 2007.

806 Canagaratna, M. R., Jimenez, J. L., Kroll, J. H., Chen, Q., Kessler, S. H., Massoli, P.,  
807 Hildebrandt Ruiz, L., Fortner, E., Williams, L. R., Wilson, K. R., Surratt, J. D.,  
808 Donahue, N. M., Jayne, J. T., and Worsnop, D. R.: Elemental ratio measurements  
809 of organic compounds using aerosol mass spectrometry: characterization,  
810 improved calibration, and implications, *Atmos. Chem. Phys.*, 15, 253–272,  
811 <https://doi.org/10.5194/acp-15-253-2015>, 2015.

812 Canonaco, F., Crippa, M., Slowik, J. G., Baltensperger, U., and Prévôt, A. S. H.: SoFi,  
813 an IGOR-based interface for the efficient use of the generalized multilinear engine  
814 (ME-2) for the source apportionment: ME-2 application to aerosol mass  
815 spectrometer data, *Atmos. Meas. Tech.*, 6, 3649–3661,  
816 <https://doi.org/10.5194/amt-6-3649-2013>, 2013.

817 Carlton, A. G., Turpin, B. J., Altieri, K. E., Seitzinger, S., Reff, A., Lim, H. J., and  
818 Ervens, B.: Atmospheric oxalic acid and SOA production from glyoxal: results of  
819 aqueous photooxidation experiments, *Atmos. Environ.*, 41, 7588–7602,  
820 <https://doi.org/10.1016/j.atmosenv.2007.05.035>, 2007.

821 Chen, C. R., Zhang, H. X., Yan, W. J., Wu, N. N., Zhang, Q., and He, K. B.: Aerosol  
822 water content enhancement leads to changes in the major formation mechanisms of  
823 nitrate and secondary organic aerosols in winter over the North China Plain,  
824 *Environ. Pollut.*, 287, 117625, <https://doi.org/10.1016/j.envpol.2021.117625>, 2021.

825 Chen, Y., Tian, M., Huang, R. J., Shi, G. M., Wang, H. B., Peng, C., Cao, J. J., Wang,  
826 Q. Y., Zhang, S. M., Guo, D. M., Zhang, L. Y., and Yang, F. M.: Characterization of  
827 urban amine-containing particles in southwestern China: seasonal variation, source,  
828 and processing, *Atmos. Chem. Phys.*, 19, 3245–3255,

829 <https://doi.org/10.5194/acp-19-3245-2019>, 2019.

830 [Chen, Y., Xie, S. D., Luo, B., and Zhai, C. Z.: Characteristics and origins of](#)  
831 [carbonaceous aerosol in the Sichuan Basin, China, \*Atmos. Environ.\*, 94, 215–223,](#)  
832 <https://doi.org/10.1016/j.atmosenv.2014.05.037>, 2014.

833 Chen, Y., Xie, S. D., Luo, B., and Zhai, C. Z.: Particulate pollution in urban  
834 Chongqing of southwest China: Historical trends of variation, chemical  
835 characteristics and source apportionment, *Sci. Total Environ.*, 584–585, 523–534,  
836 <https://doi.org/10.1016/j.scitotenv.2017.01.060>, 2017.

837 Coen, M. C., Weingartner, E., Apituley, A., Ceburnis, D., Fierz-Schmidhauser, R.,  
838 Flentje, H., Henzing, J. S., Jennings, S. G., Moerman, M., Petzold, A., Schmid, O.,  
839 and Baltensperger, U.: Minimizing light absorption measurement artifacts of the  
840 Aethalometer: Evaluation of five correction algorithms, *Atmos. Meas. Tech.*, 3,  
841 457–474, <https://doi.org/10.5194/amt-3-457-2010>, 2010.

842 Cubison, M. J., Ortega, A. M., Hayes, P. L., Farmer, D. K., Day, D., Lechner, M. J.,  
843 Brune, W. H., Apel, E., Diskin, G. S., Fisher, J. A., Fuelberg, H. E., Hecobian, A.,  
844 Knapp, D. J., Mikoviny, T., Riemer, D., Sachse, G. W., Sessions, W., Weber, R. J.,  
845 Weinheimer, A. J., Wisthaler, A., and Jimenez, J. L.: Effects of aging on organic  
846 aerosol from open biomass burning smoke in aircraft and laboratory studies, *Atmos.*  
847 *Chem. Phys.*, 11, 12049–12064, <https://doi.org/10.5194/acp-11-12049-2011>, 2011.

848 DeCarlo, P. F., Ulbrich, I. M., Crounse, J., de Foy, B., Dunlea, E. J., Aiken, A. C.,  
849 Knapp, D., Weinheimer, A. J., Campos, T., Wennberg, P. O., and Jimenez, J. L.:  
850 Investigation of the Sources and Processing of Organic Aerosol over the Central  
851 Mexican Plateau from Aircraft Measurements during MILAGRO, *Atmos. Chem.*  
852 *Phys.*, 10, 5257–5280, <https://doi.org/10.5194/acp-10-5257-2010>, 2010.

853 Drinovec, L., Močnik, G., Zotter, P., Prévôt, A. S. H., Ruckstuhl, C., Coz, E.,  
854 Rupakheti, M., Sciare, J., Müller, T., Wiedensohler, A., and Hansen, A. D. A.: The  
855 "dual-spot" Aethalometer: an improved measurement of aerosol black carbon with  
856 real-time loading compensation, *Atmos. Meas. Tech.*, 8, 1965–1979,  
857 <https://doi.org/10.5194/amt-8-1965-2015>, 2015.

858 Drozd, G. T. and McNeill, V. F.: Organic matrix effects on the formation of

859 light-absorbing compounds from  $\alpha$ -dicarbonyls in aqueous salt solution, *Environ.*  
860 *Sci.: Processes Impacts*, 16, 741–747, <https://doi.org/10.1039/c3em00579h>, 2014.

861 Elser, M., Huang, R. J., Wolf, R., Slowik, J. G., Wang, Q. Y., Canonaco, F., Li, G. H.,  
862 Bozzetti, C., Daellenbach, K. R., Huang, Y., Zhang, R. J., Li, Z. Q., Cao, J. J.,  
863 Baltensperger, U., El-Haddad, I., and Prévôt, A. S. H.: New insights into PM<sub>2.5</sub>  
864 chemical composition and sources in two major cities in China during extreme  
865 haze events using aerosol mass spectrometry, *Atmos. Chem. Phys.*, 16, 3207–3225,  
866 <https://doi.org/10.5194/acp-16-3207-2016>, 2016.

867 Ervens, B., Turpin, B. J., and Weber, R. J.: Secondary organic aerosol formation in  
868 cloud droplets and aqueous particles (aqSOA): a review of laboratory, field and  
869 model studies, *Atmos. Chem. Phys.*, 11, 11069–11102,  
870 <https://doi.org/10.5194/acp-11-11069-2011>, 2011.

871 Fountoukis, C. and Nenes, A.: ISORROPIA II: a computationally efficient  
872 thermodynamic equilibrium model for  
873  $K^+Ca^{2+}Mg^{2+}NH_4^+Na^+SO_4^{2-}NO_3^-Cl^-H_2O$  aerosols, *Atmos. Chem. Phys.*, 7,  
874 4639–4659, <https://doi.org/10.5194/acp-7-4639-2007>, 2007.

875 Fröhlich, R., Cubison, M. J., Slowik, J. G., Bukowiecki, N., Prévôt, A. S. H.,  
876 Baltensperger, U., Schneider, J., Kimmel, J. R., Gonin, M., Rohner, U., Worsnop,  
877 D. R., and Jayne, J. T.: The ToF-ACSM: a portable aerosol chemical speciation  
878 monitor with TOFMS detection, *Atmos. Meas. Tech.*, 6, 3225–3241,  
879 <https://doi.org/10.5194/amt-6-3225-2013>, 2013.

880 Gilardoni, S., Massoli, P., Paglione, M., Giulianelli, L., Carbone, C., Rinaldi, M.,  
881 Decesari, S., Sandrini, S., Costabile, F., Gobbi, G. P., Pietrogrande, M. C., Visentin,  
882 M., Scotto, F., Fuzzi, S., and Facchini, M. C.: Direct observation of aqueous  
883 secondary organic aerosol from biomass-burning emissions, *Proc. Natl. Acad. Sci.*  
884 *USA*, 113, 10013–10018, <https://doi.org/10.1073/pnas.1602212113>, 2016.

885 Guo, H. Y., Xu, L., Bougiatioti, A., Cerully, K. M., Capps, S. L., Hite Jr., J.R., Carlton,  
886 A. G., Lee, S. H., Bergin, M. H., Ng, N. L., Nenes, A., and Weber, R. J.:  
887 Fine-particle water and pH in the southeastern United States, *Atmos. Chem. Phys.*,  
888 15, 5211–5228, <https://doi.org/10.5194/acp-15-5211-2015>, 2015.

889 [Gyawali, M., Arnott, W. P., Lewis, K., and Moosmüller, H.: In situ aerosol optics in](#)  
890 [Reno, NV, USA during and after the summer 2008 California wildfires and the](#)  
891 [influence of absorbing and non-absorbing organic coatings on spectral light](#)  
892 [absorption, Atmos. Chem. Phys., 9, 8007–8015,](#)  
893 <https://doi.org/10.5194/acp-9-8007-2009>, 2009.

894 [He, M., Wang, X. R., Han, L., Feng, X. D., and M, X.: Emission Inventory of Crop](#)  
895 [Residues Field Burning and Its Temporal and Spatial Distribution in Sichuan](#)  
896 [Province, Environ. Sci., 36, 1208–1216,](#)  
897 <https://doi.org/10.13227/j.hjlx.2015.04.010>, 2015.

898 Hennigan, C. J., Izumi, J., Sullivan, A. P., Weber, R. J., and Nenes, A.: A critical  
899 evaluation of proxy methods used to estimate the acidity of atmospheric particles,  
900 Atmos. Chem. Phys., 15, 2775–2790, <https://doi.org/10.5194/acp-15-2775-2015>,  
901 2015.

902 [Hennigan, C. J., Sullivan, A. P., Collett, J. L., and Robinson, A. L.: Levoglucosan](#)  
903 [stability in biomass burning particles exposed to hydroxyl radicals, Geophys. Res.](#)  
904 [Lett., 37, L09806, https://doi.org/10.1029/2010GL043088](#), 2010.

905 Herrmann, H., Schaefer, T., Tilgner, A., Styler, S. A., Weller, C., Teich, M., and Otto,  
906 T.: Tropospheric Aqueous-Phase Chemistry: Kinetics, Mechanisms, and Its  
907 Coupling to a Changing Gas Phase, Chem. Rev., 115, 4259–4334,  
908 <https://doi.org/10.1021/cr500447k>, 2015.

909 Huang, R. J., Zhang, Y. L., Bozzetti, C., Ho, K. F., Cao, J. J., Han, Y. M., Daellenbach,  
910 K. R., Slowik, J. G., Platt, S. M., Canonaco, F., Zotter, P., Wolf, R., Pieber, S. M.,  
911 Bruns, E. A., Crippa, M., Ciarelli, G., Piazzalunga, A., Schwikowski, M.,  
912 Abbaszade, G., Schnelle-Kreis, J., Zimmermann, R., An, Z. S., Szidat, S.,  
913 Baltensperger, U., El Haddad, I., and Prevot, A. S.: High secondary aerosol  
914 contribution to particulate pollution during haze events in China, Nature, 514,  
915 218–222, <https://doi.org/10.1038/nature13774>, 2014.

916 Huang, R. J., He, Y., Duan, J., Li, Y. J., Chen, Q., Zheng, Y., Chen, Y., Hu, W. W., Lin,  
917 C. S., Ni, H. Y., Dai, W. T., Cao, J. J., Wu, Y. F., Zhang, R. J., Xu, W., Ovadnevaite,  
918 J., Ceburnis, D., Hoffmann, T., and O'Dowd, C. D.: Contrasting sources and

919 processes of particulate species in haze days with low and high relative humidity in  
920 wintertime Beijing, *Atmos. Chem. Phys.*, 20, 9101–9114,  
921 <https://doi.org/10.5194/acp-20-9101-2020>, 2020.

922 Huang, X. J., Liu, Z., Ge, Y. Z., Li, Q., Wang, X. F., Fu, H. B., Zhu, J., Zhou, B.,  
923 Wang, L., George, C., Wang, Y., Wang, X. F., Su, J. X., Xue, L. K., Yu, S. C.,  
924 Mellouki, A., and Chen, J. M.: Aerosol high water contents favor sulfate and  
925 secondary organic aerosol formation from fossil fuel combustion emissions, *npj*  
926 *Clim. Atmos. Sci.*, 6, 173, <https://doi.org/10.1038/s41612-023-00504-1>, 2023.

927 Jimenez, J. L., Canagaratna, M. R., Donahue, N. M., Prevot, A. S. H., Zhang, Q.,  
928 Kroll, J. H., DeCarlo, P. F., Allan, J. D., Coe, H., Ng, N. L., Aiken, A. C., Docherty,  
929 K. S., Ulbrich, I. M., Grieshop, A. P., Robinson, A. L., Duplissy, J., Smith, J. D.,  
930 Wilson, K. R., Lanz, V. A., Hueglin, C., Sun, Y. L., Tian, J., Laaksonen, A.,  
931 Raatikainen, T., Rautiainen, J., Vaattovaara, P., Ehn, M., Kulmala, M., Tomlinson, J.  
932 M., Collins, D. R., Cubison, M. J., Dunlea, J., Huffman, J. A., Onasch, T. B.,  
933 Alfarra, M. R., Williams, P. I., Bower, K., Kondo, Y., Schneider, J., Drewnick, F.,  
934 Borrmann, S., Weimer, S., Demerjian, K., Salcedo, D., Cottrell, L., Griffin, R.,  
935 Takami, A., Miyoshi, T., Hatakeyama, S., Shimono, A., Sun, J. Y., Zhang, Y. M.,  
936 Dzepina, K., Kimmel, J. R., Sueper, D., Jayne, J. T., Herndon, S. C., Trimborn, A.  
937 M., Williams, L. R., Wood, E. C., Middlebrook, A. M., Kolb, C. E., Baltensperger,  
938 U., and Worsnop, D. R.: Evolution of Organic Aerosols in the Atmosphere, *Science*,  
939 326, 1525–1529, <https://doi.org/10.1126/science.1180353>, 2009.

940 Kampf, C. J., Jakob, R., and Hoffmann, T.: Identification and characterization of  
941 aging products in the glyoxal/ammonium sulfate system – implications for  
942 light-absorbing material in atmospheric aerosols, *Atmos. Chem. Phys.*, 12,  
943 6323–6333, <https://doi.org/10.5194/acp-12-6323-2012>, 2012.

944 Kim, H., Collier, S., Ge, X. L., Xu, J. Z., Sun, Y. L., Jiang, W. Q., Wang, Y. L.,  
945 Herckes, P., and Zhang, Q.: Chemical processing of water-soluble species and  
946 formation of secondary organic aerosol in fogs, *Atmos. Environ.*, 200, 158–166,  
947 <https://doi.org/10.1016/j.atmosenv.2018.11.062>, 2019.

948 Kirchstetter, T. W. and Novakov T.: Evidence that the spectral dependence of light

949 absorption by aerosols is affected by organic carbon, *J. Geophys. Res.*, 109,  
950 D21208, <https://doi.org/10.1029/2004JD004999>, 2004.

951 Kondo, Y., Komazaki, Y., Miyazaki, Y., Moteki, N., Takegawa, N., Kodama, D.,  
952 Deguchi, S., Nogami, M., Fukuda, M., Miyakawa, T., Morino, Y., Koike, M.,  
953 Sakurai, H., and Ehara, K.: Temporal Variations of Elemental Carbon in Tokyo, *J.*  
954 *Geophys. Res.*, 111, D12205, <https://doi.org/10.1029/2005JD006257>, 2006.

955 Kourtchev, I., Giorio, C., Manninen, A., Wilson, E., Mahon, B., Aalto, J., Kajos, M.,  
956 Venables, D., Ruuskanen, T., Levula, J., Loponen, M., Connors, S., Harris, N.,  
957 Zhao, D. F., Kiendler-Scharr, A., Mentel, T., Rudich, Y., Hallquist, M., Doussin, J.  
958 F., Maenhaut, W., Bäck, J., Petäjä, T., Wenger, J., Kulmala, Ma., and Kalberer, M.:  
959 Enhanced Volatile Organic Compounds emissions and organic aerosol mass  
960 increase the oligomer content of atmospheric aerosols, *Sci. Rep.*, 6, 35038,  
961 <https://doi.org/10.1038/srep35038>, 2016.

962 Kroflic, A., Grilc, M., and Grgic, I.: Unraveling pathways of guaiacol nitration in  
963 atmospheric waters: nitrite, a source of reactive nitronium ion in the atmosphere,  
964 *Environ. Sci. Technol.*, 49, 9150–9158, <https://doi.org/10.1021/acs.est.5b01811>,  
965 2015.

966 [Lack, D. A., and Langridge, J. M.: On the attribution of black and brown carbon light](#)  
967 [absorption using the Ångström exponent, \*Atmos. Chem. Phys.\*, 13, 10535–10543,](#)  
968 [<https://doi.org/10.5194/acp-13-10535-2013>,](#) 2013.

969 Lanz, V. A., Alfarra, M. R., Baltensperger, U., Buchmann, B., Hueglin, C., and Prévôt,  
970 A. S. H.: Source apportionment of submicron organic aerosols at an urban site by  
971 factor analytical modelling of aerosol mass spectra, *Atmos. Chem. Phys.*, 7,  
972 1503–1522, doi:10.5194/acp-7-1503-2007, 2007.

973 Laskin, A., Laskin, J., and Nizkorodov, S. A.: Chemistry of atmospheric brown carbon,  
974 *Chem. Rev.*, 115, 4335–4382, <https://doi.org/10.1021/cr5006167>, 2015.

975 Lee, A. K., Zhao, R., Li, R., Liggio, J., Li, S. M., and Abbatt, J. P.: Formation of Light  
976 Absorbing Organo-Nitrogen Species from Evaporation of Droplets Containing  
977 Glyoxal and Ammonium Sulfate, *Environ. Sci. Technol.*, 47, 12819–12826,  
978 <https://doi.org/10.1021/es402687w>, 2013.

979 Lei, Y., Lei, X., Tian, G., Yang, J., Huang, D., Yang, X., Chen, C. C., and Zhao, J. C.:  
980 Optical Variation and Molecular Transformation of Brown Carbon During  
981 Oxidation by NO<sub>3</sub>• in the Aqueous Phase, *Environ. Sci. Technol.*, 58, 3353–3362,  
982 <https://doi.org/10.1021/acs.est.3c08726>, 2024.

983 Li, C. L., He, Q. F., Fang, Z., Brown, S. S., Laskin, A., Cohen, S. R., and Rudich, Y.:  
984 Laboratory Insights into the Diel Cycle of Optical and Chemical Transformations  
985 of Biomass Burning Brown Carbon Aerosols, *Environ. Sci. Technol.*, 54,  
986 11827–11837, <https://dx.doi.org/10.1021/acs.est.0c04310>, 2020.

987 Li, F. H., Zhou, S. Z., Du, L., Zhao, J., Hang, J., and Wang, X. M.: Aqueous-phase  
988 chemistry of atmospheric phenolic compounds: A critical review of laboratory  
989 studies, *Sci. Total Environ.*, 856, 158895,  
990 <https://doi.org/10.1016/j.scitotenv.2022.158895>, 2023.

991 Li, G., Bei, N., Tie, X., and Molina, L. T.: Aerosol effects on the photochemistry in  
992 Mexico City during MCMA-2006/MILAGRO campaign, *Atmos. Chem. Phys.*, 11,  
993 5169–5182, <https://doi.org/10.5194/acp-11-5169-2011>, 2011.

994 [Li, Z. J., Tan, H. B., Zheng, J., Liu, L., Qin, Y. M., Wang, N., Li, F., Li, Y. J., Cai, M.](#)  
995 [F., Ma, Y., and Chan, C. K.: Light absorption properties and potential sources of](#)  
996 [particulate brown carbon in the Pearl River Delta region of China, \*Atmos. Chem.\*](#)  
997 [Phys., 19, 11669–11685, <https://doi.org/10.5194/acp-19-11669-2019>, 2019.](#)

998 Lim, Y. B., Tan, Y., Perri, M. J., Seitzinger, S. P., and Turpin, B. J.: Aqueous chemistry  
999 and its role in secondary organic aerosol (SOA) formation, *Atmos. Chem. Phys.*,  
1000 10, 10521–10539, <https://doi.org/10.5194/acp-10-10521-2010>, 2010.

1001 Liu, M. X., Song, Y., Zhou, T., Xu, Z. Y., Yan, C. Q., Zheng, M., Wu, Z. J., Hu, M.,  
1002 Wu, Y. S., and Zhu, T.: Fine particle pH during severe haze episodes in northern  
1003 China, *Geophys. Res. Lett.*, 44, 5213–5221, <https://doi.org/10.1002/2017gl073210>,  
1004 2017.

1005 [Liu, Y., Huang, R. J., Lin, C. S., Yuan, W., Li, Y. J., Zhong, H. B., Yang, L., Wang, T.,](#)  
1006 [Huang, W., Xu, W., Huang, D. D., and Huang, C.: Nitrate-Photolysis Shortens the](#)  
1007 [Lifetimes of Brown Carbon Tracers from Biomass Burning, \*Environ. Sci. Technol.\*,](#)  
1008 [59, 640–649, <https://doi.org/10.1021/acs.est.4c06123>, 2024.](#)

1009 Lorenzo, R. A. D., Washenfelder, R. A., Attwood, A. R., Guo, H., Xu, L., Ng, N. L.,  
1010 Weber, R. J., Baumann, K., Edgerton, E., and Young, C. J.:  
1011 Molecular-Size-Separated Brown Carbon Absorption for Biomass-Burning Aerosol  
1012 at Multiple Field Sites, *Environ. Sci. Technol.*, 51, 3128–3137,  
1013 <https://doi.org/10.1021/acs.est.6b06160>, 2017.

1014 Lu, Z., Streets, D. G., Winijkul, E., Yan, F., Chen, Y., Bond, T. C., Feng, Y., Dubey, M.  
1015 K., Liu, S., Pinto, J. P., and Carmichael, G. R.: Light absorption properties and  
1016 radiative effects of primary organic aerosol emissions, *Environ. Sci. Technol.*, 49,  
1017 4868–4877, <https://doi.org/10.1021/acs.est.5b00211>, 2015.

1018 [Luo, J. Q., Zhang, J. K., Huang, X. J., Liu, Q., Luo, B., Zhang, W., Rao, Z. H., and](#)  
1019 [Yu, Y. C.: Characteristics, evolution, and regional differences of biomass burning](#)  
1020 [particles in the Sichuan Basin, China, \*J. Environ. Sci.\*, 89, 35–46,](#)  
1021 [<https://doi.org/10.1016/j.jes.2019.09.015>, 2020.](#)

1022 Matthew, B. M., Middlebrook, A. M., and Onasch, T. B.: Collection Efficiencies in an  
1023 Aerodyne Aerosol Mass Spectrometer as a Function of Particle Phase for  
1024 Laboratory Generated Aerosols, *Aerosol Sci. Technol.*, 42, 884–898,  
1025 <https://doi.org/10.1080/02786820802356797>, 2008.

1026 McNeill, V. F.: Aqueous Organic Chemistry in the Atmosphere: Sources and Chemical  
1027 Processing of Organic Aerosols, *Environ. Sci. Technol.*, 49, 1237–1244,  
1028 <https://doi.org/10.1021/es5043707>, 2015.

1029 Meng, J. J., Liu, X. D., Hou, Z. F., Yi, Y. A., Yan, L., Li, Z., Cao, J. J., Li, J. J., and  
1030 Wang, G. H.: Molecular characteristics and stable carbon isotope compositions of  
1031 dicarboxylic acids and related compounds in the urban atmosphere of the North  
1032 China Plain: Implications for aqueous phase formation of SOA during the haze  
1033 periods, *Sci. Total Environ.*, 705, 135256,  
1034 <https://doi.org/10.1016/j.scitotenv.2019.135256>, 2020.

1035 Middlebrook, A. M., Bahreini, R., Jimenez, J. L., and Canagaratna, M. R.: Evaluation  
1036 of Composition-Dependent Collection Efficiencies for the Aerodyne Aerosol Mass  
1037 Spectrometer using Field Data, *Aerosol Sci. Technol.*, 46, 258–271,  
1038 <https://doi.org/10.1080/02786826.2011.620041>, 2012.

1039 Ministry of Environmental Protection (MEP): P.R. Of China, China National Ambient  
1040 Air Quality Standard (GB 3095-2012), [http://kjs.mep.  
1041 gov.cn/hjbhzbz/bzwb/dqhjbh/dqhjzlbz/201203/t20120302\\_224165.htm](http://kjs.mep.gov.cn/hjbhzbz/bzwb/dqhjbh/dqhjzlbz/201203/t20120302_224165.htm), 2012.

1042 Moosmüller, H., Chakrabarty, R. K., and Arnott, W. P.: Aerosol light absorption and  
1043 its measurement: A review, *J. Quant. Spectrosc. Ra.*, 110, 844–878,  
1044 <https://doi.org/10.1016/j.jqsrt.2009.02.035>, 2009.

1045 Ng, N. L., Canagaratna, M. R., Jimenez, J. L., Chhabra, P. S., Seinfeld, J. H., and  
1046 Worsnop, D. R.: Changes in organic aerosol composition with aging inferred from  
1047 aerosol mass spectra, *Atmos. Chem. Phys.*, 11, 6465–6474,  
1048 <https://doi.org/10.5194/acp-11-6465-2011>, 2011a.

1049 Ng, N. L., Canagaratna, M. R., Jimenez, J. L., Zhang, Q., Ulbrich, I. M., and Worsnop,  
1050 D. R.: Real-Time Methods for Estimating Organic Component Mass  
1051 Concentrations from Aerosol Mass Spectrometer Data, *Environ. Sci. Technol.*, 45,  
1052 910–916, <https://doi.org/10.1021/es102951k>, 2011b.

1053 Ng, N. L., Canagaratna, M. R., Zhang, Q., Jimenez, J. L., Tian, J., Ulbrich, I. M.,  
1054 Kroll, J. H., Docherty, K. S., Chhabra, P. S., Bahreini, R., Murphy, S. M., Seinfeld,  
1055 J. H., Hildebrandt, L., Donahue, N. M., DeCarlo, P. F., Lanz, V. A., Prévôt, A. S. H.,  
1056 Dinar, E., Rudich, Y., and Worsnop, D. R.: Organic aerosol components observed  
1057 in Northern Hemispheric datasets from Aerosol Mass Spectrometry, *Atmos. Chem.  
1058 Phys.*, 10, 4625–4641, <https://doi.org/10.5194/acp-10-4625-2010>, 2010.

1059 Ng, N. L., Herndon, S. C., Trimborn, A., Canagaratna, M. R., Croteau, P. L., Onasch,  
1060 T. B., Sueper, D., Worsnop, D. R., Zhang, Q., Sun, Y. L., and Jayne J. T.: An  
1061 Aerosol Chemical Speciation Monitor (ACSM) for Routine Monitoring of the  
1062 Composition and Mass Concentrations of Ambient Aerosol, *Aerosol Sci. Technol.*,  
1063 45, 780–794, <https://doi.org/10.1080/02786826.2011.560211>, 2011c.

1064 Nguyen, T. K. V., Zhang, Q., Jimenez, J. L., Pike, M., and Carlton, A. G.: Liquid  
1065 Water: Ubiquitous Contributor to Aerosol Mass, *Environ. Sci. Technol. Lett.*, 3,  
1066 257–263, <https://doi.org/10.1021/acs.estlett.6b00167>, 2016.

1067 Nozière, B., and Esteve, W.: Light-absorbing aldol condensation products in acidic  
1068 aerosols: Spectra, kinetics, and contribution to the absorption index, *Atmos.*

1069 Environ., 41, 1150–1163, <https://doi.org/10.1016/j.atmosenv.2006.10.001>, 2007.

1070 Nozière, B., Dziedzic, P., and Córdova, A.: Products and Kinetics of the Liquid-Phase  
1071 Reaction of Glyoxal Catalyzed by Ammonium Ions (NH<sub>4</sub><sup>+</sup>), *J. Phys. Chem. A*, 113,  
1072 231–237, <https://doi.org/10.1021/jp8078293>, 2009.

1073 Ortega, A. M., Ortega, D. A., Cubison, M. J., Brune, W. H., Bon, D., Gouw de, J. A.,  
1074 and Jimenez, J. L.: Secondary organic aerosol formation and primary organic  
1075 aerosol oxidation from biomass-burning smoke in a flow reactor during FLAME-3,  
1076 *Atmos. Chem. Phys.*, 13, 11551–11571,  
1077 <https://doi.org/10.5194/acp-13-11551-2013>, 2013.

1078 Ortiz-Montalvo, D. L., Lim, Y. B., Perri, M. J., Seitzinger, S. P., and Turpin, B. J.:  
1079 Volatility and Yield of Glycolaldehyde SOA Formed through Aqueous  
1080 Photochemistry and Droplet Evaporation, *Aerosol Sci. Technol.*, 46, 1002–1014,  
1081 <https://doi.org/10.1080/02786826.2012.686676>, 2012.

1082 Paatero, P.: The Multilinear Engine: A Table-Driven, Least Squares Program for  
1083 Solving Multilinear Problems, Including the n-Way Parallel Factor Analysis Model,  
1084 *J. Comput. Graph. Stat.*, 8, 854–888,  
1085 <https://doi.org/10.1080/10618600.1999.10474853>, 1999.

1086 Paatero, P. and Hopke, P. K.: Discarding or downweighting high-noise variables in  
1087 factor analytic models, *Anal. Chim. Acta.*, 490, 277–289,  
1088 [https://doi.org/10.1016/S0003-2670\(02\)01643-4](https://doi.org/10.1016/S0003-2670(02)01643-4), 2003.

1089 Paatero, P. and Tapper, U.: Positive matrix factorization: A non-negative factor model  
1090 with optimal utilization of error estimates of data values, *Environmetrics*, 5,  
1091 111–126, <https://doi.org/10.1002/env.3170050203>, 1994.

1092 Paglione, M., Gilardoni, S., Rinaldi, M., Decesari, S., Zanca, N., Sandrini, S.,  
1093 Giulianelli, L., Bacco, D., Ferrari, S., Poluzzi, V., Scotto, F., Trentini, A., Poulain,  
1094 L., Herrmann, H., Wiedensohler, A., Canonaco, F., Prévôt, A. S. H., Massoli, P.,  
1095 Carbone, C., Facchini, M. C., and Fuzzi, S. C.: The impact of biomass burning and  
1096 aqueous-phase processing on air quality: a multi-year source apportionment study  
1097 in the Po Valley, Italy, *Atmos. Chem. Phys.*, 20, 1233–1254,  
1098 <https://doi.org/10.5194/acp-20-1233-2020>, 2020.

1099 Pang, H. W., Zhang, Q., Lu, X. H., Li, K. N., Chen, H., Chen, J. M., Yang, X., Ma, Y.  
1100 G., Ma, J. L., and Huang, C.: Nitrite-Mediated Photooxidation of Vanillin in the  
1101 Atmospheric Aqueous Phase, *Environ. Sci. Technol.*, 53, 14253–14263,  
1102 <https://doi.org/10.1021/acs.est.9b03649>, 2019.

1103 [Peng, C., Tian, M., Chen, Y., Wang, H. B., Zhang, L. M., Shi, G. M., Liu, Y., Yang, F.](#)  
1104 [M., and Zhai, C. Z.: Characteristics, Formation Mechanisms and Potential](#)  
1105 [Transport Pathways of PM<sub>2.5</sub> at a Rural Background Site in Chongqing, Southwest](#)  
1106 [China, \*Aerosol Air Qual. Res.\*, 19, 1980–1992,](#)  
1107 <https://doi.org/10.4209/aaqr.2019.01.0010>, 2019.

1108 Peng, C., Tian, M., Shi, G. M., Zhang, S. M., Long, X., Che, H. X., Zhong, J., You, X.  
1109 Y., Bao, Z. E., Yang, F. M., Qi, X., Zhai, C. Z., and Chen, Y.: Sources and light  
1110 absorption of brown carbon in urban areas of the Sichuan Basin, China:  
1111 Contribution from biomass burning and secondary formation, *Atmos. Res.*, 318,  
1112 107992, <https://doi.org/10.1016/j.atmosres.2025.107992>, 2025.

1113 Powelson, M. H., Espelien, B. M., Hawkins, L. N., Galloway, M. M., and Haan, D. O.  
1114 D.: Brown Carbon Formation by Aqueous-Phase Carbonyl Compound Reactions  
1115 with Amines and Ammonium Sulfate, *Environ. Sci. Technol.*, 48, 985–993,  
1116 <https://doi.org/10.1021/es4038325>, 2014.

1117 Qin, Y. M., Tan, H. B., Li, Y. J., Li, Z. J., Schurman, M. I., Liu, L., Wu, C., and Chan,  
1118 C. K.: Chemical characteristics of brown carbon in atmospheric particles at a  
1119 suburban site near Guangzhou, China, *Atmos. Chem. Phys.*, 18, 16409–16418,  
1120 <https://doi.org/10.5194/acp-18-16409-2018>, 2018.

1121 Saleh, R., Hennigan, C. J., McMeeking, G. R., Chuang, W. K., Robinson, E. S., Coe,  
1122 H., Donahue, N. M., and Robinson, A. L.: Absorptivity of brown carbon in fresh  
1123 and photo-chemically aged biomass-burning emissions, *Atmos. Chem. Phys.*, 13,  
1124 7683–7693, <https://doi.org/10.5194/acp-13-7683-2013>, 2013.

1125 Saleh, R., Robinson, E. S., Tkacik, D. S., Ahern, A. T., Liu, S., Aiken, A. C., Sullivan,  
1126 R. C., Presto, A. A., Dubey, M. K., Yokelson, R. J., Donahue, N. M., and Robinson,  
1127 A. L.: Brownness of organics in aerosols from biomass burning linked to their  
1128 black carbon content, *Nat. Geosci.*, 7, 647–650, <https://doi.org/10.1038/ngeo2220>,

1129 2014.

1130 Sareen, N., Moussa, S. G., and McNeill, V. F.: Photochemical Aging of  
1131 Light-Absorbing Secondary Organic Aerosol Material, *J. Phys. Chem. A*, 117,  
1132 2987–2996, <https://doi.org/10.1021/jp309413j>, 2013.

1133 Shrivastava, M., Cappa, C. D., Fan, J. W., Goldstein, A. H., Guenther, A. B., Jimenez,  
1134 J. L., Kuang, C. A., Laskin, A., Martin, S. T., Ng, N. L., Petaja, T., Pierce, J. R.,  
1135 Rasch, P. J., Roldin, P., Seinfeld, J. H., Shilling, J., Smith, J. N., Thornton, J. A.,  
1136 Volkamer, R., Wang, J., Worsnop, D. R., Zaveri, R. A., Zelenyuk, A., and Zhang,  
1137 Q.: Recent advances in understanding secondary organic aerosol: Implications for  
1138 global climate forcing, *Rev. Geophys.*, 55, 509–559, doi:10.1002/2016RG000540,  
1139 2017.

1140 Sun, Y. L., Du, W., Fu, P. Q., Wang, Q. Q., Li, J., Ge, X. L., Zhang, Q., Zhu, C. M.,  
1141 Ren, L. J., Xu, W. Q., Zhao, J., Han, T. T., Worsnop, D. R., and Wang, Z. F.:  
1142 Primary and secondary aerosols in Beijing in winter: sources, variations and  
1143 processes, *Atmos. Chem. Phys.*, 16, 8309–8329,  
1144 <https://doi.org/10.5194/acp-16-8309-2016>, 2016a.

1145 Sun, Y. L., Jiang, Q., Xu, Y. S., Ma, Y., Zhang, Y. J., Liu, X. G., Li, W. J., Wang, F., Li,  
1146 J., Wang, P. C., and Li, Z. Q.: Aerosol characterization over the North China Plain:  
1147 Haze life cycle and biomass burning impacts in summer, *J. Geophys. Res.: Atmos.*,  
1148 121, 2508–2521, <https://doi.org/10.1002/2015jd024261>, 2016b.

1149 Sun, Y. L., Zhang, Q., Anastasio, C., and Sun, J.: Insights into secondary organic  
1150 aerosol formed via aqueous-phase reactions of phenolic compounds based on high  
1151 resolution mass spectrometry, *Atmos. Chem. Phys.*, 10, 4809–4822,  
1152 <https://doi.org/10.5194/acp-10-4809-2010>, 2010.

1153 Tan, Y., Lim, Y. B., Altieri, K. E., Seitzinger, S. P., and Turpin, B. J.: Mechanisms  
1154 leading to oligomers and SOA through aqueous photooxidation: insights from OH  
1155 radical oxidation of acetic acid and methylglyoxal, *Atmos. Chem. Phys.*, 12,  
1156 801–813, <https://doi.org/10.5194/acp-12-801-2012>, 2012.

1157 Tao, J., Gao, J., Zhang, L., Zhang, R., Che, H., Zhang, Z., Lin, Z., Jing, J., Cao, J., and  
1158 Hsu, S. C.: PM<sub>2.5</sub> pollution in a megacity of southwest China: source

1159 apportionment and implication, *Atmos. Chem. Phys.*, c14, 8679–8699,  
1160 <https://doi.org/10.5194/acp-14-8679-2014>, 2014.

1161 Tian M., Liu Y., Yang F. M., Zhang L. M., Peng C., Chen Y., Shi G. M., Wang H. B.,  
1162 Luo B., Jiang C. T., Li B., Takeda N., and Koizumi K.: Increasing importance of  
1163 nitrate formation for heavy aerosol pollution in two megacities in Sichuan Basin,  
1164 southwest China, *Environ. Pollut.*, 250, 898–905,  
1165 <https://doi.org/10.1016/j.envpol.2019.04.098>, 2019.

1166 Wang, G. H., Zhang, R. Y., Gomez, M. E., Yang, L. X., Zamora, M. L., Hu, M., Lin,  
1167 Y., Peng, J. F., Guo, S., Meng, J. J., Li, J. J., Cheng, C. L., Hu T. F., Ren, Y. Q.,  
1168 Wang, Y. S., Gao, J., Cao, J. J., An, Z. S., Zhou, W. J., Li, G. H., Wang, J. Y., Tian,  
1169 P. F., Marrero-Ortiz, W., Secret, J., Du, Z. F., Zheng, J., Shang, D. J., Zeng, L. M.,  
1170 Shao, M., Wang, W. G., Huang, Y., Wang, Y., Zhu, Y. J., Li, Y. X., Hu, J. X., Pan,  
1171 B., Cai, L., Cheng, Y. T., Ji, Y. M., Zhang, F., Rosenfeld, D., Liss, P. S., Duce, R. A.,  
1172 Kolb, C. E., and Molina, M. J.: Persistent sulfate formation from London Fog to  
1173 Chinese haze, *Proc. Natl. Acad. Sci. USA*, 113, 13630–13635,  
1174 <https://doi.org/10.1073/pnas.1616540113>, 2016.

1175 Wang, H. B., Tian, M., Chen, Y., Shi, G. M., Liu, Y., Yang, F. M., Zhang, L. M., Deng,  
1176 L. Q., Yu, J. Y., Peng, C., and Cao, X. Y.: Seasonal characteristics, formation  
1177 mechanisms and source origins of PM<sub>2.5</sub> in two megacities in Sichuan Basin, China,  
1178 *Atmos. Chem. Phys.*, 18, 865–881, <https://doi.org/10.5194/acp-18-865-2018>, 2018.

1179 [Wang, H. B., Zhang, L. M., Huo, T. T., Wang, B., Yang, F. M., Chen, Y., Tian, M.,](#)  
1180 [Qiao, B. Q., and Peng, C.: Application of parallel factor analysis model to](#)  
1181 [decompose excitation-emission matrix fluorescence spectra for characterizing](#)  
1182 [sources of water-soluble brown carbon in PM<sub>2.5</sub>, \*Atmos. Environ.\*, 223, 117192,](#)  
1183 [<https://doi.org/10.1016/j.atmosenv.2019.117192>, 2019a.](#)

1184 Wang, J. F., Ye, J. H., Zhang, Q., Zhao, J., Wu, Y. Z., Li, J. Y., Liu, D. T., Li, W. J.,  
1185 Zhang, Y. G., Wu, C., Xie, C. H., Qin, Y. M., Lei, Y. L., Huang, X. P., Guo, J. P.,  
1186 Liu, P. F., Fu, P. Q., Li, Y. J., Lee, H. C., Choi, H., Zhang, J., Liao, H., Chen, M. D.,  
1187 Sun, Y. L., Ge, X. L., Martin, S. T., and Jacob, D. J.: Aqueous production of  
1188 secondary organic aerosol from fossil-fuel emissions in winter Beijing haze, *Proc.*

1189 Natl. Acad. Sci. USA, 118, e2022179118, <https://doi.org/10.1073/pnas.2022179118>,  
1190 2021.

1191 Wang, Q. Y., Ye, J. H., Wang, Y. C., Zhang, T., Ran, W. K., Wu, Y. F., Tian, J., Li, L.,  
1192 Zhou, Y. Q., Ho, H. S. S., Dang, B., Zhang, Q., Zhang, R. J., Chen, Y., Zhu, C. S.,  
1193 and Cao, J. J.: Wintertime Optical Properties of Primary and Secondary Brown  
1194 Carbon at a Regional Site in the North China Plain, *Environ. Sci. Technol.*, 53,  
1195 12389–12397, <https://doi.org/10.1021/acs.est.9b03406>, 2019<sup>b</sup>.

1196 Washenfelder, R. A., Attwood, A. R., Brock, C. A., Guo, H., Xu, L., Weber, R. J., Ng,  
1197 N. L., Allen, H. M., Ayres, B. R., Baumann, K., Cohen, R. C., Draper, D. C.,  
1198 Duffey, K. C., Edgerton, E., Fry, J. L., Hu, W. W., Jimenez, J. L., Palm, B. B.,  
1199 Romer, P., Stone, E. A., Wooldridge, P. J., and Brown, S. S.: Biomass burning  
1200 dominates brown carbon absorption in the rural southeastern United States,  
1201 *Geophys. Res. Lett.*, 42, 653–664, <https://doi.org/10.1002/2014gl062444>, 2015.

1202 Wu, C. and Yu, J. Z.: Determination of primary combustion source organic  
1203 carbon-to-elemental carbon (OC/EC) ratio using ambient OC and EC  
1204 measurements: Secondary OC-EC correlation minimization method, *Atmos. Chem.*  
1205 *Phys.*, 16, 5453–5465, <https://doi.org/10.5194/acp-16-5453-2016>, 2016.

1206 Wu, H., Peng, C., Zhai, T. Y., Deng, J. C., Lu, P. L., Li, Z. L., Chen, Y., Tian, M., Bao,  
1207 Z. E., Long, X., Yang, F. M., and Zhai, C. Z.: Characteristics of light absorption  
1208 and environmental effects of Brown carbon aerosol in Chongqing during summer  
1209 and winter based on online measurement: Implications of secondary formation,  
1210 *Atmos. Environ.*, 338, 120843, <https://doi.org/10.1016/j.atmosenv.2024.120843>,  
1211 2024.

1212 Xie, C. H., Xu, W. Q., Wang, J. F., Wang, Q. Q., Liu, D. T., Tang, G. Q., Chen, P., Du,  
1213 W., Zhao, J., Zhang, Y. J., Zhou, W., Han, T. T., Bian, Q. Y., Li, J., Fu, P. Q., Wang,  
1214 Z. F., Ge, X. L., Allan, J., Coe, H., and Sun, Y. L.: Vertical characterization of  
1215 aerosol optical properties and brown carbon in winter in urban Beijing, China,  
1216 *Atmos. Chem. Phys.*, 19, 165–179, <https://doi.org/10.5194/acp-19-165-2019>, 2019.

1217 Xu, B. Q., Zhang, G., Gustafsson, Ö., Kawamura, K., Li, J., Andersson, A., Bikkina,  
1218 S., Kunwar, B., Pokhrel, A., Zhong, G. C., Zhao, S. Z., Li, J., Huang, C., Cheng, Z.

1219 N., Zhu, S. Y., Peng, P. A., and Sheng, G. Y.: Large contribution of fossil-derived  
1220 components to aqueous secondary organic aerosols in China, *Nat. Commun.*, 13,  
1221 5115, <https://doi.org/10.1038/s41467-022-32863-3>, 2022.

1222 Xu, W. Q., Han, T. T., Du, W., Wang, Q. Q., Chen, C., Zhao, J., Zhang, Y. J., Li, J., Fu,  
1223 P. Q., Wang, Z. F., Worsnop, D. R., and Sun, Y. L.: Effects of Aqueous-Phase and  
1224 Photochemical Processing on Secondary Organic Aerosol Formation and Evolution  
1225 in Beijing, China, *Environ. Sci. Technol.*, 51, 762–770,  
1226 <https://doi.org/10.1021/acs.est.6b04498>, 2017.

1227 Xu, W. Q., Sun, Y. L., Chen, C., Du, W., Han, T. T., Wang, Q. Q., Fu, P. Q., Wang, Z.  
1228 F., Zhao, X. J., Zhou, L. B., Ji, D. S., Wang, P. C., and Worsnop, D. R.: Aerosol  
1229 composition, oxidation properties, and sources in Beijing: results from the 2014  
1230 Asia-Pacific Economic Cooperation summit study, *Atmos. Chem. Phys.*, 15,  
1231 13681–13698, <https://doi.org/10.5194/acp-15-13681-2015>, 2015.

1232 Xu, W. Q., Sun, Y. L., Wang, Q. Q., Zhao, J., Wang, J. F., Ge, X. L., Xie, C. J., Zhou,  
1233 W., Du, W., Li, J., Fu, P. Q., Wang, Z. F., Worsnop, D. R., and Coe, H.: Changes in  
1234 Aerosol Chemistry From 2014 to 2016 in Winter in Beijing: Insights From  
1235 High-Resolution Aerosol Mass Spectrometry, *J. Geophys. Res.: Atmos.*, 124,  
1236 1132–1147, <https://doi.org/10.1029/2018JD029245>, 2019.

1237 Yan, C. Q., Zheng, M., Bosch, C., Andersson, A., Desyaterik, Y., Sullivan, A. P.,  
1238 Collett, J. L., Zhao, B., Wang, S. X., He, K. B., and Gustafsson, Ö.: Important  
1239 fossil source contribution to brown carbon in Beijing during winter, *Sci. Rep.*, 7,  
1240 43182, <https://doi.org/10.1038/srep43182>, 2017.

1241 Yang, J. W., Au, W. C., Law, H., Lam, C. H., and Nah, T.: Formation and evolution of  
1242 brown carbon during aqueous-phase nitrate-mediated photooxidation of guaiacol  
1243 and 5-nitroguaiacol, *Atmos. Environ.*, 254, 118401,  
1244 <https://doi.org/10.1016/j.atmosenv.2021.118401>, 2021.

1245 Yang, F. M., Tan, J., Zhao, Q., Du, Z., He, K. B., Ma, Y. L., Duan, F. K., Chen, G., and  
1246 Zhao, Q.: Characteristics of PM<sub>2.5</sub> speciation in representative megacities and  
1247 across China, *Atmos. Chem. Phys.*, 11, 5207–5219,  
1248 <https://doi.org/10.5194/acp-11-5207-2011>, 2011.

1249 Ye, Z. L., Qu, Z. X., Ma, S. S., Luo, S. P., Chen, Y. T., Chen, H., Chen, Y. F., Zhao, Z.  
1250 Z., Chen, M. D., and Ge, X. L.: A comprehensive investigation of aqueous-phase  
1251 photochemical oxidation of 4-ethylphenol, *Sci. Total Environ.*, 685, 976–985,  
1252 <https://doi.org/10.1016/j.scitotenv.2019.06.276>, 2019.

1253 Yokelson, R. J., Urbanski, S. P., Atlas, E. L., Toohey, D. W., Alvarado, E. C., Crouse,  
1254 J. D., Wennberg, P. O., Fisher, M. E., Wold, C. E., Campos, T. L., Adachi, K.,  
1255 Buseck, P. R., and Hao, W. M.: Emissions from forest fires near Mexico City,  
1256 *Atmos. Chem. Phys.*, 7, 5569–5584, <https://doi.org/10.5194/acp-7-5569-2007>,  
1257 2007.

1258 Yu, L., Smith, J., Laskin, A., Anastasio, C., Laskin, J., Zhang, Q.: Chemical  
1259 characterization of SOA formed from aqueous-phase reactions of phenols with the  
1260 triplet excited state of carbonyl and hydroxyl radical, *Atmos. Chem. Phys.*, 14,  
1261 13801–13816, <https://doi.org/10.5194/acp-14-13801-2014>, 2014.

1262 Yu, L., Smith, J., Laskin, A., George, K. M., Anastasio, C., Laskin, J., Dillner, A. M.,  
1263 and Zhang, Q.: Molecular transformations of phenolic SOA during photochemical  
1264 aging in the aqueous phase: competition among oligomerization, functionalization,  
1265 and fragmentation, *Atmos. Chem. Phys.*, 16, 4511–4527,  
1266 <https://doi.org/10.5194/acp-16-4511-2016>, 2016.

1267 [Zhang, X. Y., Liu, H. X., Cheng, J. L., Song, W., Wang, H. C., Zhang, Y. L., and Wang,](#)  
1268 [X. M.: Gas-Phase Oxidation of Guaiacol by NO<sub>3</sub> Radicals: Kinetic Measurements](#)  
1269 [and Implications, ACS ES&T Air, 2, 903–910,](#)  
1270 [<https://doi.org/10.1021/acsestair.4c00353>, 2025.](#)

1271 Zhao, J., Du, W., Zhang, Y. J., Wang, Q. Q., Chen, C., Xu, W. Q., Han, T. T., Wang, Y.  
1272 Y., Fu, P. Q., Wang, Z. F., Li, Z. Q., and Sun, Y. L.: Insights into aerosol chemistry  
1273 during the 2015 China Victory Day parade: results from simultaneous  
1274 measurements at ground level and 260 m in Beijing, *Atmos. Chem. Phys.*, 17,  
1275 3215–3232, <https://doi.org/10.5194/acp-17-3215-2017>, 2017.

1276 Zhao, J., Qiu, Y. M., Zhou, W., Xu, W. Q., Wang, J. F., Zhang, Y. J., Li, L. J., Xie, C.  
1277 H., Wang, Q. Q., Du, W., Worsnop, D. R., Canagaratna, M. R., Zhou, L. B., Ge, X.  
1278 L., Fu, P. Q., Li, J., Wang, Z. F., Donahue, N. M., and Sun, Y. L.: Organic Aerosol

1279 Processing During Winter Severe Haze Episodes in Beijing, *J. Geophys. Res.:*  
1280 *Atmos.*, 124, 10248–10263, <https://doi.org/10.1029/2019JD030832>, 2019.

1281 Zhao, R., Lee, A. K. Y., Huang, L., Li, X., Yang, F., and Abbatt, J. P. D.:  
1282 Photochemical processing of aqueous atmospheric brown carbon, *Atmos. Chem.*  
1283 *Phys.*, 15, 6087–6100, <https://doi.org/10.5194/acp-15-6087-2015>, 2015.

1284 Zhao, R., Mungall, E. L., Lee, A. K. Y., Aljawhary, D., and Abbatt, J. P. D.:  
1285 Aqueous-phase photooxidation of levoglucosan – a mechanistic study using  
1286 aerosol time-of-flight chemical ionization mass spectrometry (Aerosol ToF-CIMS),  
1287 *Atmos. Chem. Phys.*, 14, 9695–9706, <https://doi.org/10.5194/acp-14-9695-2014>,  
1288 2014.

1289 Zhong, H. B., Huang, R. J., Chang, Y. H., Duan, J., Lin, C. S., and Chen, Y.:  
1290 Enhanced formation of secondary organic aerosol from photochemical oxidation  
1291 during the COVID-19 lockdown in a background site in Northwest China, *Sci.*  
1292 *Total Environ.*, 778, 144947, <https://doi.org/10.1016/j.scitotenv.2021.144947>,  
1293 2021.

1294 Zhu, C. S., Cao, J. J., Hu, T. F., Shen, Z. X., Tie, X. X., Huang, H., Wang, Q. Y.,  
1295 Huang, R. J., Zhao, Z. Z., Mocnik, G., and Hansen, A. D. A.: Spectral dependence  
1296 of aerosol light absorption at an urban and a remote site over the Tibetan Plateau,  
1297 *Sci. Total Environ.*, 590–591, 14–21,  
1298 <https://doi.org/10.1016/j.scitotenv.2017.03.057>, 2017.

1299 [Zhu, L. W., Cui, Y. J., Ge, X. L., Ye, Z. I., and Zhao, Z. Z.: Aqueous-phase](#)  
1300 [photochemical oxidation of extracted WSOC in PM<sub>2.5</sub> from biomass burning,](#)  
1301 [China Environ. Sci.](#), 43, 1014–1025,  
1302 <https://doi.org/10.19674/j.cnki.issn1000-6923.20220928.004>, 2023.